

## Laser-induced fluorescence diagnostics of the cross-field discharge of Hall thrusters

This article has been downloaded from IOPscience. Please scroll down to see the full text article.

2013 Plasma Sources Sci. Technol. 22 013001

(<http://iopscience.iop.org/0963-0252/22/1/013001>)

View [the table of contents for this issue](#), or go to the [journal homepage](#) for more

Download details:

IP Address: 163.9.19.90

The article was downloaded on 30/11/2012 at 12:20

Please note that [terms and conditions apply](#).

## INVITED REVIEW

# Laser-induced fluorescence diagnostics of the cross-field discharge of Hall thrusters

Stéphane Mazouffre

ICARE, CNRS, 1C avenue de la Recherche Scientifique, 45071 Orléans, France

E-mail: [stephane.mazouffre@cnrs-orleans.fr](mailto:stephane.mazouffre@cnrs-orleans.fr)

Received 20 August 2012, in final form 17 October 2012

Published 29 November 2012

Online at [stacks.iop.org/PSST/22/013001](http://stacks.iop.org/PSST/22/013001)

## Abstract

This article presents a review of work performed over the past ten years in France, centered on the utilization of laser-induced fluorescence (LIF) spectroscopy to diagnose the low-pressure magnetized dc discharge of a Hall thruster (HT). The latter is a gridless electric propulsion device in a crossed electric and magnetic field configuration, which is used onboard satellites and space probes for various types of maneuvers. Although the design of a HT is relatively simple, the physical mechanisms that govern thrust generation and efficiency are not yet fully understood. Characterization of the ion and atom velocity distribution function (VDF) appears to be a powerful way to obtain insights into the underlying physics. The VDF of xenon and krypton—the most common propellants—is therefore locally interrogated by means of LIF on excited levels. In this review emphasis is placed on time-averaged and time-resolved continuous-wave LIF measurements, associated quantities and recent outcomes. Results will be presented concerning a variety of phenomena: velocity vector field structuring, ion population interaction, electric field generation, ion magnetic drift, apparent atom acceleration, interaction of the plasma plume with background gas and low-frequency electric field oscillations, to name only a few.

(Some figures may appear in colour only in the online journal)

## 1. Introduction

In comparison with chemical engines, electric propulsion systems offer significant advantages for commercial and scientific space missions in terms of payload mass, launch cost and mission duration due to a fast propellant ejection speed that warrants a large propellant mass saving according to the Tsiolkovsky rocket equation [1]. Nowadays the most important application of electric propulsion systems is the north–south station keeping of geosynchronous telecommunication satellites. The increase in electrical power available onboard the spacecraft will lead to new applications of electric propulsion systems in the near future, such as orbit raising and orbit topping maneuvers, orbit transfer maneuvers, not only in the Earth upper atmosphere but also toward far-off planets and asteroids, as well as end-of-life deorbiting. Many different electric propulsion technologies exist: arcjets [2], magnetoplasmadynamic thrusters [2], gridded ion engines [2, 3], Hall thrusters [2, 4], helicon

thruster [5], VASIMR [6], PEGASES thruster [7] and so on. Among all the different electric propulsion devices, two technologies, namely the gridded ion engine (GIE) and the Hall thruster (HT), are at the present time mature with a long flight heritage. For instance, over 200 HTs have been flown on satellites since 1971. GIEs are characterized by a purely electrostatic acceleration of ions, the latter being extracted from a plasma through a set of high-voltage grids [3]. The discharge in a GIE can be generated by electron bombardment, microwave power or radio-frequency power. In contrast, HTs are gridless engines. They provide thrust by acceleration of ions in a low pressure discharge in a crossed electric and magnetic field configuration [4]. The two technologies exhibit a similar thrust efficiency that can be as high as 70% at high power. GIEs are characterized by a high specific impulse, which means a great ion ejection velocity, and a relatively low thrust level. HTs provide a relatively large thrust with a moderate specific impulse. However, the thrust-to-power ratio of HTs is more than three times larger than

that of GIEs [9]. Furthermore, a HT is simple, compact and robust. Therefore, Hall thrusters represent an attractive electric propulsion technology for standard maneuvers as well as for foreseen new applications for which thrust is a critical issue.

Despite dozens of years of HT development and investigation, many physical mechanisms that govern the behavior and the performance of such a magnetized discharge are nevertheless ill-understood and not well quantified. Among others one can cite the electron diffusion across the magnetic barrier, plasma–wall interactions, energy losses and geometrical and size effects. This lack of knowledge is clearly a limiting factor for various aspects of the technology: optimization of existing HTs, derivation of scaling laws and sizing methodologies, utilization of alternative propellants, for example. Moreover, this situation slows down the construction of novel and more efficient thruster architectures and the development of predictive numerical models. Among the possible experimental approaches to gain knowledge, the fine examination of ion and atom transport phenomena in a HT appears to be a powerful way to improve our understanding of the underlying physics in this specific type of magnetized plasma source. The transport properties of xenon and krypton atoms and ions—these two gases being the most common propellant for electric thrusters—can be accurately examined through the measurement of a statistical quantity, the so-called velocity distribution function (VDF). The  $Xe I$  and  $Kr I$  atom and  $Xe II$  and  $Kr II$  ion VDF can be probed in a non-intrusive way by means of laser-induced fluorescence (LIF) spectroscopy with a continuous-wave (CW) light beam in the near-infrared spectral domain.

This review focuses on the utilization of LIF spectroscopy for HT diagnosis and how it gives insights into the physics at work in the cross-field discharge and plume of the device. The contribution, which in fact covers ten years of research performed at the CARE Institute in France, is divided into several parts. In section 2, a brief overview is offered on HT principle, design and operation. Typical discharge parameters are also given to localize this device in the vast collection of plasma sources. The LIF spectroscopy method is presented in section 3. After explaining the principle of the technique, we discuss the optical train and the data acquisition system for time-averaged measurements. In addition, optical transitions used for probing HT discharge with xenon and krypton are introduced. After describing the basics of the cw-LIF technique, section 4 is about fluorescence line shape properties and origin, and ion VDF extraction. Section 5 outlines computation of macroscopic quantities from the measured VDF. The ion velocity, velocity dispersion and vector field are discussed in this section. Calculation of the accelerating electric field distribution is illustrated in section 6. Direct determination from the velocity profile is compared with a method based on the moments of Boltzmann's equation. Although weakly magnetized, ions undergo an azimuthal drift due to the magnetic field as illustrated in section 7. The effect of the external cathode on the ion drift is also investigated in this section. In section 8, we take an interest in the atomic transport properties. In contrast to

the ion case, the atom velocity is obtained from fluorescence lineshape modeling. Invasion of the beam by the neutral gas and ion recombination at the walls is shown to play a key role in the atom velocity development. Section 9 discusses time-resolved LIF measurements using a photon-counting technique. Time-varying ion VDFs are shown. In this section, low-frequency spatio-temporal oscillations of the electric field are experimentally evidenced. Finally, conclusions are drawn in section 10 and comments on future possibilities are given to close this review.

## 2. HT physics and functioning

A HT is an advanced propulsion device for spacecrafts that uses an electric discharge with magnetized electrons to ionize and accelerate a propellant gas [2, 4, 8]. HTs offer interesting features in terms of thrust-to-power ratio, specific impulse, efficiency, lifetime and mass. They are therefore recognized as an attractive propulsion means for space missions and maneuvers that require a large velocity increment. Currently, 1 to 2 kW-class HTs are employed for geosynchronous satellite attitude correction and station keeping. They also appear as good candidates for the primary propulsion engine of space probes, as demonstrated by the successful SMART-1 Moon flyby solar-powered mission [10]. Space agencies together with satellite manufacturers and users nonetheless envisage new fields of application for electric propulsion systems that require low- and high-power devices. Low-power HTs ( $\sim 100$  W) are well suited for drag compensation of observation satellites that operate on a low-altitude orbit in the Earth's atmosphere as well as for trajectory correction of small platforms and microsatellite constellations. The use of mid-power ( $\sim 5$  kW) HTs for orbit raising, orbit topping and even full orbit transfer maneuvers of communication satellites would offer significant benefits in terms of launch mass, payload mass and operational life. Finally, ambitious robotic missions such as exploration of the outer planets of the solar system and far-off comets as well as transfer of cargo vehicles to support crewed missions require very high power electric propulsion systems to overcome velocity increments that can be as large as several tens of  $\text{km s}^{-1}$ . That is the reason why a significant part of research activities focuses on building and testing of HTs with power above 10 kW with a thrust level larger than 1 N [9].

In contrast to, e.g., gridded ion engines, in a HT, acceleration of heavy atomic ions to high velocity occurs within the core of the discharge, which implies the use of a magnetized plasma to sustain internal electric fields. A schematic of a HT is depicted in figure 1. The principle relies upon a magnetic barrier and a low pressure dc discharge generated between an external cathode and an anode in such a way that a crossed electric and magnetic field discharge is created [4, 11–13]. The anode, which often serves as a gas injector, is located at the upstream end of a coaxial annular dielectric channel that confines the discharge. Xenon is generally used as a propellant gas due to its specific properties in terms of high atomic mass and low ionization energy. A set of solenoids or permanent magnets provides a radially

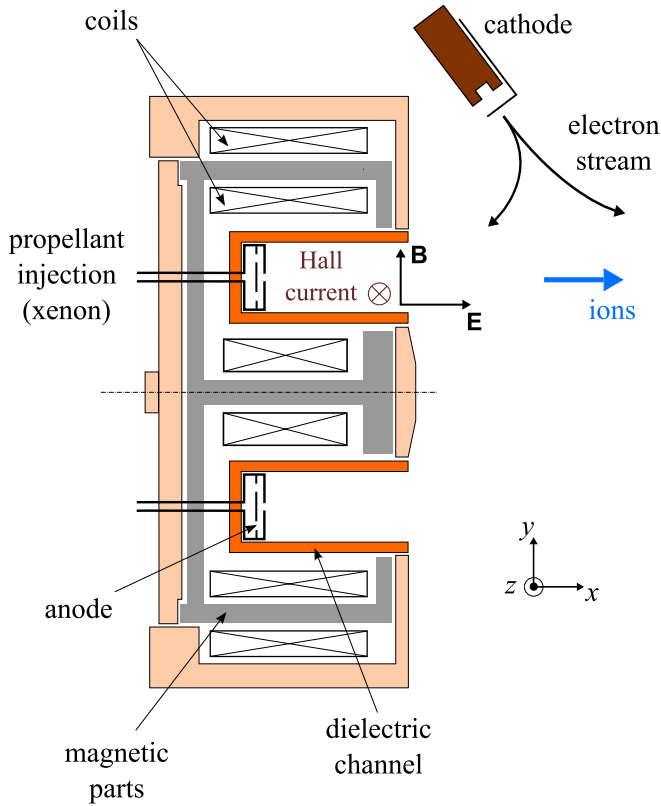


**Figure 1.** Cross-section view of a HT body in the  $x$ - $y$  plane. The magnetic and electric field vectors as well as the Hall current are indicated.

directed magnetic field  $B$  the strength of which is maximum in the vicinity of the channel exhaust. The magnetic field is chosen strong enough to make the electron Larmor radius much smaller than the discharge chamber length, but weak enough not to affect ion trajectories. The electric potential drop is mostly concentrated in the final section of the channel owing to the low electron axial mobility in this restricted area. The corresponding induced local axial electric field  $E$  has two main effects. First, it drives a high electron azimuthal drift—the Hall current—that is responsible for the efficient ionization of the supplied gas. Second, it accelerates ions out of the channel, which generates thrust. The ion beam is neutralized by a fraction of electrons emitted from the cathode. When operating near 1.5 kW, a HT ejects ions at  $20 \text{ km s}^{-1}$  and generates 90 mN of thrust with an overall efficiency of about 50%. The main elements of the thruster assembly are displayed in the drawing of figure 1 as well as in the photograph of figure 2. Figure 3 shows the 20 kW-class PPS20k-ML thruster firing with xenon for several discharge powers.

For the record, typical parameters and quantities are given in table 1 for a 1.5 kW-class HT equipped with BN-SiO<sub>2</sub> walls and operating with xenon. As can be seen, electrons are magnetized whereas ions are not. The electron temperature is far above characteristic values encountered in low-pressure discharges; the electron density is also large. As a consequence, the ionization degree is high: in terms of flux, more than 90% of the injected gas flow is ionized in the discharge of a HT. Note that the HT that circulates in the

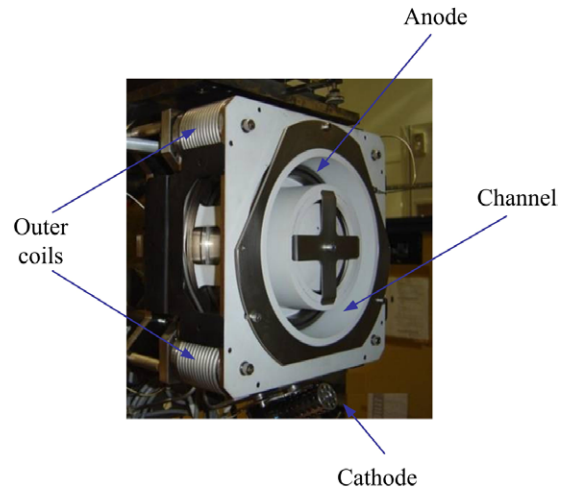


**Figure 2.** Picture of the 5 kW-class PPSX@000-ML HT prior to testing. The main thruster elements are shown.

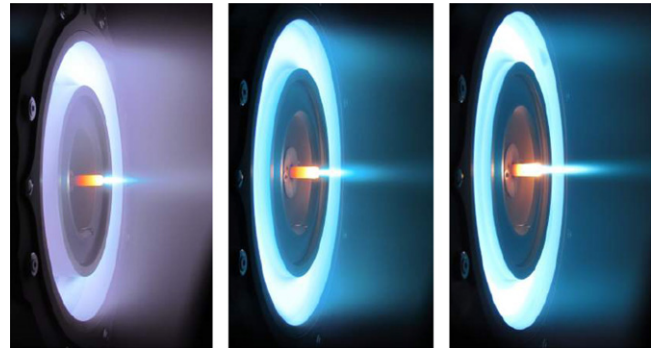


**Figure 3.** Photograph of the PPS20k-ML HT with its centered mounted cathode firing with xenon in the Pivoine-2G test chamber [9]. From left to right: low power, 15 kW, and 23.5 kW.

high  $B$  field region is always far above the discharge current ( $I_{\text{Hall}} \approx 40 \text{ A}$  using data in table 1).

### 3. LIF diagnostic technique

#### 3.1. Method

LIF spectroscopy is a non-intrusive diagnostic tool that enables one to determine the velocity of probed particles along the laser beam direction by measuring the Doppler shift of absorbed photons [14–16]. The most common optical transitions used for measuring the atom and ion velocity in the discharge and plume of a HT are summarized in table 2. All wavelengths lie in the red and near-infrared range of the electromagnetic spectrum as laser excitation always starts from an excited state. Measuring the frequency at which the laser beam energy is absorbed allows one to determine the atom or ion Doppler shift. Therefore, it is possible to calculate the velocity component corresponding to the laser beam direction using the following equations:

$$\Delta\nu = \nu - \nu_0 = \frac{1}{2\pi} \mathbf{k} \cdot \mathbf{v} \quad \text{and} \quad v_k = c \frac{(\nu - \nu_0)}{\nu}, \quad (1)$$

where  $\Delta\nu$  is the Doppler shift,  $\mathbf{k}$  is the laser beam wave vector,  $\mathbf{v}$  is the probed particle velocity vector,  $c$  is the speed of light

**Table 1.** Typical values for the characteristic parameters of a 1.5 kW-class HT equipped with BN-SiO<sub>2</sub> walls and operating with xenon.  $d$  correspond to the channel mean diameter.  $T$ ,  $I_{sp}$  and  $\eta$  refer to the thrust, specific impulse and anode efficiency, respectively.  $v_{drift}$  is the electron azimuthal velocity. Other symbols have their usual meaning.

1.5 kW-class Hall thruster				
Dimension	Input	Output	Quantity	Quantity
$d = 80$ mm	$\dot{m}_{Xe} = 5$ mg s <sup>-1</sup>	$T = 85$ mN	$B_{max} = 200$ G	$n_a = 10^{19}$ m <sup>-3</sup>
$r_{L,e} = 1$ mm	$U_d = 300$ V	$I_{sp} = 1700$	$E_{max} = 350$ V cm <sup>-1</sup>	$n_e = 5 \times 10^{17}$ m <sup>-3</sup>
$r_{L,i} = 100$ mm	$I_d = 4.5$ A	$\eta = 0.55$	$v_{drift} = 2 \times 10^6$ m s <sup>-1</sup>	$T_e = 30$ eV

**Table 2.** Current excitation and fluorescence wavelengths in LIF studies on HTs.

Species	Initial level	$\lambda_{exc}$ (nm)	$\lambda_{fluo}$ (nm)	Reference
Xe II	5d <sup>4</sup> D <sub>7/2</sub>	605.11	529.22	[25]
Xe II	5d <sup>2</sup> F <sub>7/2</sub>	834.72	541.91	[17, 26]
Xe I	6s [1/2] <sub>2</sub> <sup>0</sup> (1s <sub>2</sub> )	834.68	473.41	[27]
Xe I	6s [3/2] <sub>2</sub> <sup>0</sup> (1s <sub>5</sub> )	823.16	823.16	[27]
Kr II	4d <sup>4</sup> F <sub>7/2</sub>	820.27	462.92	[23]
Kr II	5d <sup>4</sup> D <sub>7/2</sub>	728.98	473.90	[28]

in vacuum,  $v_k$  is the velocity parallel to  $k$ ,  $\nu_0$  is the studied transition unshifted frequency, and  $\nu$  is the recorded frequency.

### 3.2. Optical train and detection branch

Several configurations of the LIF optical bench used to determine ion and atom velocity in the channel and plume of HTs and derived concepts can be found in, e.g., [17–22]. As an example we describe here the optical bench available to our team for time-averaged LIF experiments on HT discharges [17, 18, 23]. The laser beam used to excite metastable and resonant levels of atoms and ions is produced by an amplified tunable single-mode external cavity laser diode that can deliver up to 700 mW of power in the 810–840 nm spectral domain. The laser remains mode-hop free over a frequency tuning range of more than 10 GHz. The spectral width of the laser beam profile is about 1 MHz. Behind the tapered amplifier the laser beam passes through a Faraday isolator to prevent optical feedback into the laser cavity. The wavelength is accurately measured by means of a calibrated wavemeter whose absolute accuracy is 80 MHz ( $\approx 60$  m s<sup>-1</sup>). A scanning confocal Fabry–Pérot interferometer with a 1 GHz free spectral range is used to real-time check the quality of the laser mode and to detect mode hops. The power of the beam is also continuously monitored. The primary laser beam is modulated by a mechanical chopper at a frequency  $\sim 1$  kHz before being coupled into a single-mode optical fiber of 5  $\mu$ m core diameter. The fiber allows one to carry the beam into the vacuum chamber. A schematic of the optical bench is shown in figure 4.

As illustrated in figure 5, several laser injection schemes are possible. As the ion acceleration process and the atom flow occur mostly in the direction of the thruster axis, see figure 3, the axial velocity component is the first component to be monitored. The laser beam can be shone from the back of the channel through a dedicated orifice (figure 5(a)). Another possibility is to shine the laser beam from the front (figure 5(b)). In that case some optical components are introduced into the

ion beam. This option nevertheless allows measurements at various radial positions [20, 23]. The laser beam can also propagate in the vertical ( $y$ ) or horizontal ( $z$ ) plane to access the radial or azimuthal velocity component (figure 5(c)). Naturally, a combination of laser injection geometries is possible to offer multi-dimensional diagnostics of the HT plasma, e.g. a 2D map ( $v_x, v_y$ ) of the velocity [16, 24]. There are also various possibilities for the collection optics. The detection branch can be placed perpendicular to the laser axis. In that case, the interior of the channel can solely be examined through a slit made in the channel external wall, see figure 5(a). As shown in figure 5(b), the optics can also be oriented at an oblique angle relative to the laser direction to offer the possibility to enter the channel. For investigation of the PPS®X000-ML and PPS100-ML thruster discharge, the single-mode fiber output was located behind the thruster to inject the beam through a small orifice realized in the back of the channel [17, 18]. Power deposition in the measurement volume must be well controlled. In most experiments, the laser power density reaches a few mW mm<sup>-2</sup>, which warrants a weak saturation effect on the studied transition. A detection branch of 40 mm focal length, which focuses the fluorescence light onto a 200  $\mu$ m core diameter optical fiber, is mounted onto a travel stage perpendicular to the channel axis. The magnification ratio is 1, meaning that the spatial resolution is 200  $\mu$ m in the axial direction. A slit several mm in length was made in the channel dielectric outer wall in order to carry out measurements inside the channel. The collection system allows us in fact to probe the entire acceleration region. The fluorescent light transported by the 200  $\mu$ m fiber is focused onto the entrance slit of a 20 cm focal length monochromator that isolates the fluorescence line from the rest of the spectrum. A narrow-bandwidth interference filter can be used instead [23]. A photomultiplier tube (PMT) serves as a light detector. For time-averaged LIF measurements, a lock-in amplifier operating at the chopper frequency is used to discriminate the fluorescence light from the intrinsic plasma emission. Scanning of the laser diode cavity, data acquisition and laser wavelength monitoring are of course computer controlled.

### 3.3. Optical transitions

The most common excitation and fluorescence wavelengths used in LIF studies on HT plasma are shown in table 2. The laser wavelength is in the red or the near-infrared spectral domain as optical pumping starts from a metastable level or the resonant 1s<sub>2</sub> level. In a HT discharge, both the electron density

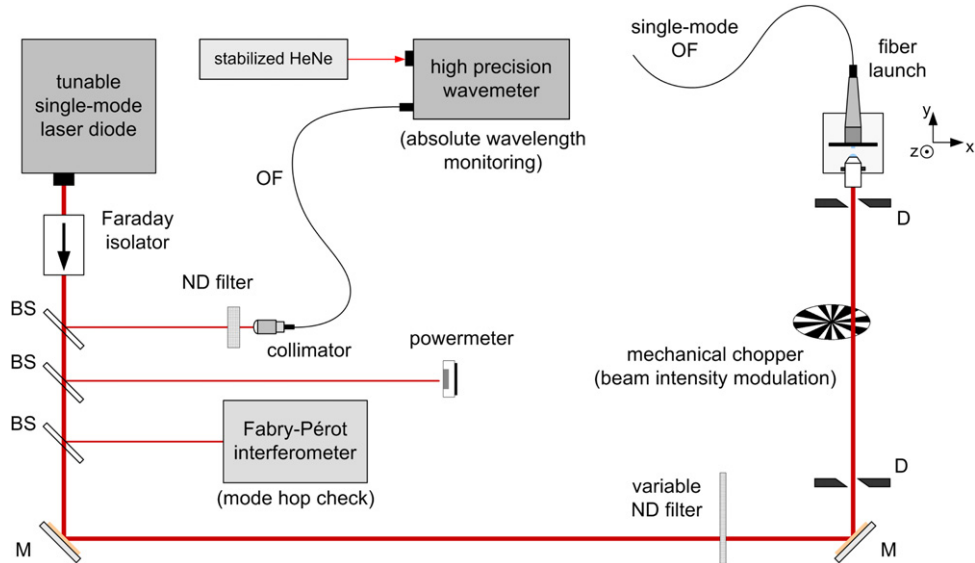


**Figure 4.** Diagram of a CW LIF optical bench (BS: beam splitter, ND: neutral density, M: mirror, D: diaphragm, OF: optical fiber).

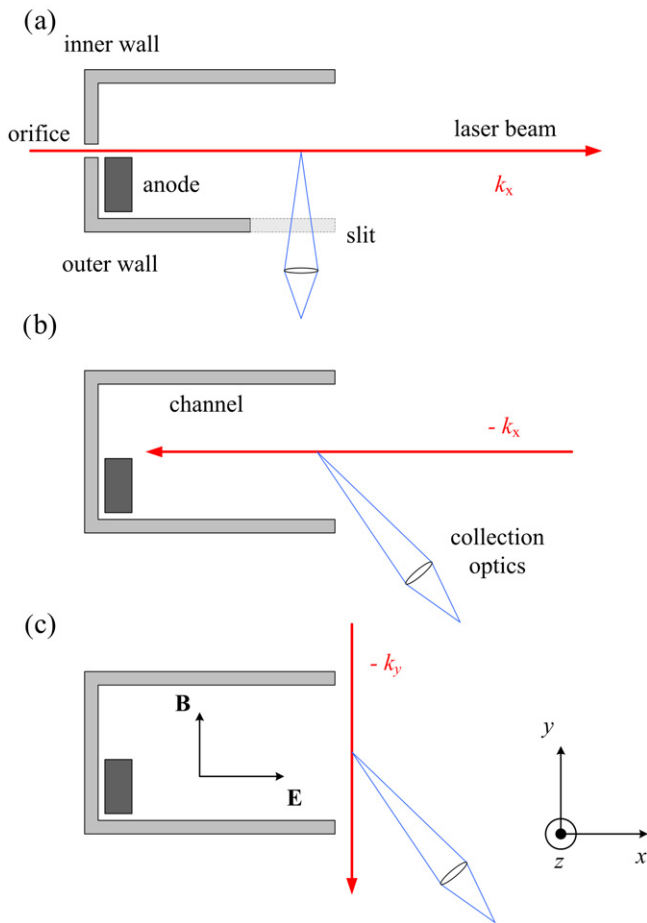


**Figure 5.** Examples of LIF injection geometry and detection branch configurations.

and temperature are large, hence the corona approximation, i.e. direct excitation by electron impact, holds. As a consequence the VDF of the excited state resembles to a large extent that of ground-state atoms and ions, which are the most populated states. Examination of atom and ion velocity is therefore

considerably simplified since detection of atomic species in the electronic ground-state necessitates either a LIF scheme with XUV photons or a two-photon LIF scheme in the VUV range [15]. The 605 nm light is obtained with a ring-dye laser. All other wavelengths are produced with a compact solid-state diode laser. Fluorescence radiation is in the visible range but, in the case of the resonant scheme for Xe atoms, in the metastable  $1s_5$  level. Fluorescence wavelengths are selected according to their branching ratio in order to ensure a large photon flux.

## 4. Velocity distribution function

### 4.1. Fluorescence line shape

In a LIF experiment, the spectral line shape is a convolution of the probed species VDF with the absorption line shape and the laser frequency profile [14, 15]. The laser linewidth is below 1 MHz with a CW source, therefore it can be considered as a Dirac delta function and subsequently neglected. Mechanisms at the origin of the absorption line shape in a HT discharge have been described in detail in many publications, see, e.g., [17, 18, 28]. We here review and briefly explain absorption line shape broadening effects. Xenon has seven abundant isotopes, two of which have a non-zero nuclear spin. Krypton has five abundant isotopes, one of which has a non-zero nuclear spin. Even and odd isotopes lead, respectively, to an isotopic shift and a hyperfine structure [26]. An absorption line is then composed of several optical transitions. For instance, the overall isotope and hyperfine structure for the  $\text{Kr II } 4d^4F_{7/2} \rightarrow 5p^2D_{5/2}^o$  at the 820.273 nm line comprises 22 transitions. The Doppler broadening of each transition is relatively low as the gas temperature is typically around 600 K in a HT plasma. The 834.7 nm Xe II and the 820.3 nm Kr II line profiles were measured by LIF in a low-pressure radiofrequency discharge at room temperature [23]. The full-width at half-maximum (FWHM) of the recorded spectra is  $\Delta\nu \approx 0.79$  GHz for Kr II and  $\Delta\nu \approx 0.61$  GHz for Xe II. It corresponds to a dispersion

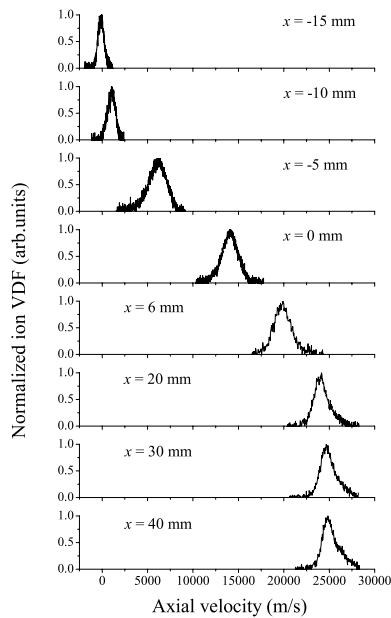


**Figure 6.** Normalized Xe II ion VDFs measured by means of LIF spectroscopy at 834.7 nm along the channel axis of the PPS@X000-ML HT operating at 500 V [17]. The position  $x = 0$  mm corresponds to the channel exit plane.

in velocity of  $650 \text{ m s}^{-1}$  and  $510 \text{ m s}^{-1}$  for Kr II and Xe II, respectively. In the case of the cross-field discharge of a HT, two other broadening mechanisms must be taken into account. Due to the applied steady magnetic field, an optical transition experiences the Zeeman effect, which leads to a splitting of all levels into manifold sub-levels [29, 30]. In addition, as isotopes have a slightly different atomic mass, electrostatic acceleration of ions leads to a dispersion in velocity [17]. Finally, saturation effect induced by the laser beam power must be considered [15]. With a power density around  $1 \text{ mW mm}^{-2}$ , saturation of the natural line shape is, however, weak both for ion and atom optical transitions.

As we shall see in section 5, all the aforementioned effects cannot explain the shape of the observed Xe II and Kr II ion line profiles in the course of the flow. For example, in the region of strong magnetic field wherein the Zeeman effect is large, the width of a recorded Xe II fluorescence profile is typically between  $3000 \text{ m s}^{-1}$  and  $7000 \text{ m s}^{-1}$ , far above the theoretical value ( $\approx 1500 \text{ m s}^{-1}$ ) [31]. The broadening of the ion fluorescence line shape in fact mostly originates in a mechanism intrinsic to the physics at work. It is so important that no deconvolution procedure is applied. The measured fluorescence profile is therefore assumed to image the local ion VDF. The case of atoms is somewhat different. The isotopic shift, hyperfine structure, Doppler effect and Zeeman splitting must be accounted for. As we shall see, retrieval of the atomic VDF requires an accurate modeling of the measured line profile [27]. Details are given in section 8.

#### 4.2. Ion VDF

A series of raw Xe II ion axial VDFs is shown in figure 6. All VDFs were measured along the channel axis of the 5 kW-class PPS@X000-ML thruster operating at 500 V [17, 31]. Ions are

created at rest in the interior of the discharge chamber. They are accelerated through the magnetic barrier where electron confinement induces a large electric field. In this example, the acceleration layer extends from  $x = -10$  mm up to  $x = 30$  mm. As can be seen in figure 6, the shape of the Xe II ion VDF changes when moving downstream. The distribution broadens in the course of the ion flow. The origin of the broadening is examined in detail in the next section. A slow wing appears inside the channel whereas a fast wing is visible at the end of the acceleration region. The on-axis development of the ion VDF is typical for HTs. It has been observed with other thrusters and also when krypton is used as the propellant. However, the trend illustrated in figure 6 can be altered by charge-exchange (CEX) and momentum transfer collisions with atoms of the residual gas when the pressure is high. A thorough analysis of the background pressure impact of the ion VDF has been performed using LIF by Nackles and Hargus with a low-power thruster [32]. Time-averaged ion VDFs are at present well reproduced through computer simulations with a hybrid code [33]. Comparison between experimental and numerical velocity distributions allowed one to refine the model of a HT plasma. Moreover, with this approach one was able to obtain an accurate electron mobility profile throughout the transverse magnetic field, which supports the hypothesis of turbulent anomalous electron transport [33].

At the end of the acceleration process, a significant fraction of Xe II ions exhibit an axial velocity component above the theoretical limit, as illustrated in figure 6. For a discharge voltage of 500 V, the maximum achievable velocity is  $26890 \text{ m s}^{-1}$ . Oscillations in time of the electric field with frequencies that correspond to the reciprocal of the ion transit time across the acceleration layer generate such supra-spiced-up ions [17]. In contrast, slow ions are also produced in such a way that the average kinetic energy of the ion fluid always stays below the electrical potential energy. The two specific kinds of ions are in fact created by way of a wave-riding mechanism that occurs when ion motion and field oscillations are synchronized. Note that the existence of supra-spiced-up ions behind the acceleration region of a HT is predicted by computer simulations carried out with a hybrid model [34] and a particle-in-cell model [35].

Figure 7 shows the contour plot in a 1D-phase space ( $x, v_x$ ) of the normalized Kr II ion axial VDF along the channel axis of the permanent magnet PPI HT [36] firing with a discharge voltage of 200 V [23]. Four different ion groups are clearly identified. The main branch labeled (1) corresponds to ions that accelerate from  $5000 \text{ m s}^{-1}$  in the channel exit plane up to  $16000 \text{ m s}^{-1}$  at 100 mm. These ions are created inside the channel and they experience the whole potential drop. This group is also the one described in figure 6. The second branch (2) is located where the electric field is too low to accelerate ions to very high velocity. This group corresponds to ions coming from the opposite side of the annular channel and interacting with the main ion beam. The apparent acceleration is a mere geometric effect. It results from the axial velocity component of the divergent velocity ion population. The third branch (3) appears with velocity from  $0 \text{ m s}^{-1}$  at 10 mm up to  $10000 \text{ m s}^{-1}$  at 50 mm. The slow ions

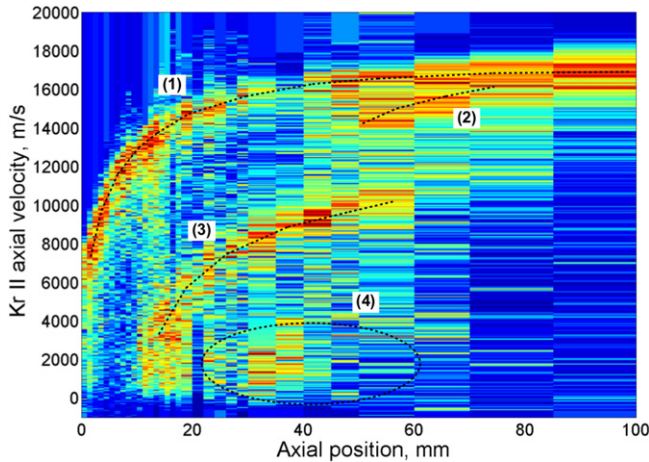


**Figure 7.** Kr II axial VDF along the channel axis of the PPI thruster (200 V) [23].

originate either from CEX collisions between the main beam (1) or the diverging beam (2) and background residual gas or cathode gas, or from local ionization. Slow ions are produced close to the channel exit plane where densities are large. They are subsequently accelerated as the electric field stretches out up to  $x = 60$  mm. Beyond 60 mm, the third branch (3) is lost in the background noise. The last group (4) is observed with velocities varying between 0 and  $4000 \text{ m s}^{-1}$ . It corresponds to slow ions that are created at locations too far away from the channel exit plane to be strongly influenced by the electric field. This ion population may result from local ionization or interaction between beams from various parts of the channel. There is no significant acceleration and the ions propagate axially at a constant velocity  $\approx 1000 \text{ m s}^{-1}$  that remains in the range of the ion-acoustic velocity. An identical picture is obtained when the PPI thruster is operated with xenon [23]. Note that the origin of branches (3) and (4) is not yet clear. Further experiments are necessary to obtain an undisputed explanation.

Figure 8 is a contour plot of the Xe II axial VDF measured along the centerline of the PPI thruster at 200 V [23]. The ion velocity varies from  $-4000 \text{ m s}^{-1}$  behind the exit plane up to  $14000 \text{ m s}^{-1}$  at  $x = 100$  mm. The negative velocity ion group corresponds to ions produced at rest in front of the thruster and accelerated through the potential drop between the plume and the source. To ensure the negative velocity was not due to a beam reflection, the measurement was repeated, placing a small tilted mirror on the thruster center to avoid a counterpropagating ( $-k$  vector) laser beam. The potential drop is only of a few volts. However, the kinetic energy of these ions is large enough to generate sputtering of the central part of the thruster. The apparent Xe II ion acceleration in figure 8 is again a geometrical effect. The observed axial velocity is related to the projection along the laser beam axis, which is merged with the thruster centerline of the velocity vector of ion population from all elementary sections of the annular channel. It reveals the relatively large divergence angle of the ion beam of a HT [8]. An identical picture is obtained when the PPI thruster is operated with krypton [23].

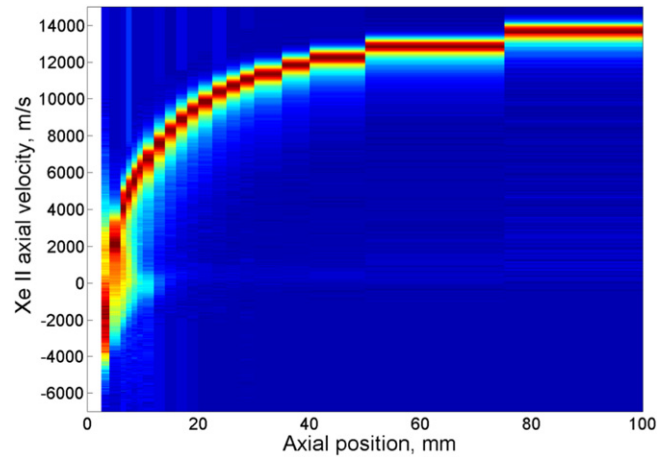


**Figure 8.** Xe II axial VDF along the PPI thruster centerline (200 V) [23].

Figures 7 and 8 reveal the complexity of the ion flow pattern in the plume of a HT. VDFs with a complicated shape are formed as a distinct ion population interacts and overlaps due to acceleration, local production by ionization and/or collision events and elementary beam interaction. The specific features of the HT plume dynamics have also been investigated by Hargus and Charles with the 200 W BHT-200 thruster [37]. For instance, they observed multiple velocity component distributions and mixing of velocity groups behind the channel exhaust. Two points are worth noting here. First, the high quality of detail that can be found in previous figures unambiguously demonstrates the value of the cw-LIF technique. Second, rich ion VDF pictures and associated physical mechanisms are easier to observe with small size HTs since the distances to cover to catch all phenomena are shorter.

So far, only axial ion VDFs have been presented. The ion velocity can also be measured in the radial direction. The optical bench is similar to that described in section 3.2 with a transverse injection geometry, see figure 5. The two velocity components can be acquired at the same time if the main beam is split into two light beams modulated at two different frequencies. Two locking amplifiers are then necessary to simultaneously capture the LIF signals [38]. The Xe II ion radial velocity was measured in the near-field plume of several thrusters: the 5 kW-class Russian SPT140 [38] thruster, the 200 W BHT-200 [39] and the 600 W BHT-600 [20] thrusters from the Busek company. Contour plots of the axial and radial VDFs sampled at a single cross section approximately 0.6 diameters downstream of the BHT-200-X3 HT are shown in figure 9 [37, 39]. The thruster was fired with xenon at 250 V. The axial velocity distribution is the broadest on the plume centerline ( $y = 0$ ). This results from the interaction between ions that flow from all elementary sections of the annular channel. The radial velocity distribution in figure 9 is also broad. Divergence toward and away from the plume center is visible. Around the plume center ( $y = 0$ ) there is a large number of ions with a slow radial velocity component. The existence of ions with a null radial velocity on the thruster axis is difficult to understand. It could, however, be the signature for an ion electrostatic shock wave in a collisionless medium [40]

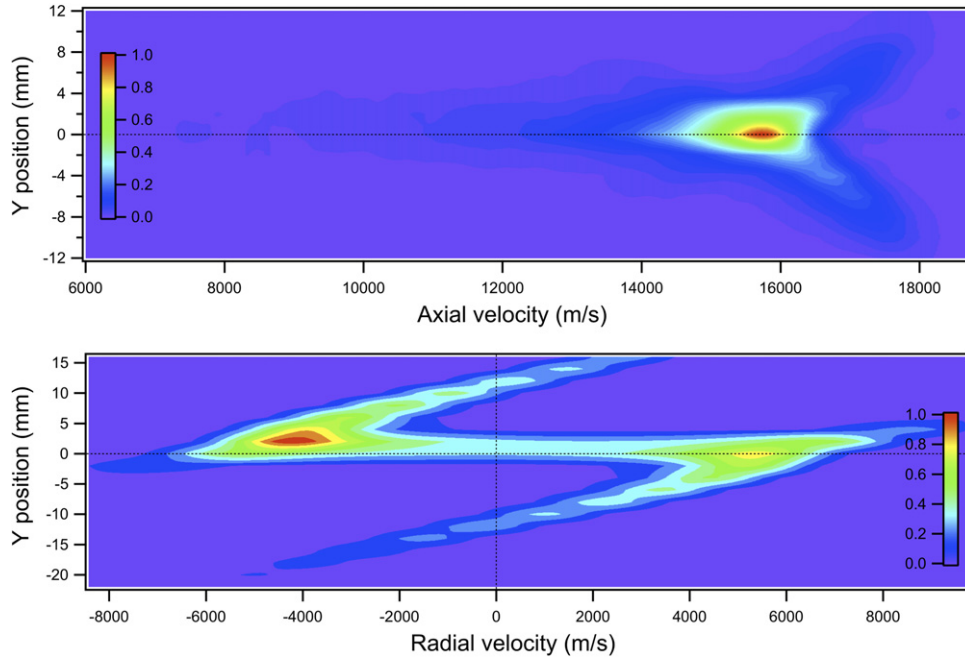


**Figure 9.** Xe II axial (top) and radial (bottom) VDF at various  $y$  coordinates near the exit plane of the BHT-200-X3 thruster [39].  $y = 0$  is the thruster axis.

when supersonic ion beams interact. In figure 9, the ion flow is not perfectly symmetrical as the two radial velocities are not equal ( $-4200 \text{ m s}^{-1}$  against  $+5200 \text{ m s}^{-1}$ ). The average total ion velocity magnitude is  $16390 \text{ m s}^{-1}$  in this example.

## 5. Velocity and dispersion profiles

### 5.1. Macroscopic quantities

Instead of analyzing in detail time-averaged ion VDFs, which is a cumbersome task, albeit one full of insights, one can study statistical quantities inferred directly from the measured velocity distributions.

- The most probable velocity  $v_{\text{mp}}$  is the highest value of the distribution function.
- The mean velocity  $\bar{v}$  is obtained from the first-order moment of the velocity distribution.
- The velocity spread or dispersion  $\sigma$  corresponds to the standard deviation; it is computed from the second-order moment of the distribution. The  $p$  parameter is another way to define the velocity dispersion. It reads

$$p = 2\sqrt{2 \text{Ln}(2)} \times \sigma \approx 2.335 \times \sigma, \quad (2)$$

where  $\sigma$  is the standard deviation. The quantity  $p$  is equal to the FWHM in the case of a Gaussian distribution.

Other macroscopic quantities can be defined. The so-called maximum ion velocity  $v_{\text{max}}$  corresponds to the velocity for which the amplitude of the distribution drops down to a given percentage of its maximum value on the high-velocity side. A 10% factor was chosen by Gawron and co-workers for two reasons, namely [18] (i) it permits an unambiguous definition of  $v_{\text{max}}$  as the true maximum velocity is difficult to determine, and (ii) the fraction of ions moving with the  $v_{\text{max}}$  velocity

is significant. A similar definition could be applied for a minimum velocity. An ion temperature  $T$  can also be assessed from the dispersion  $\sigma$ . The relation between  $T$  and  $\sigma$  is given by

$$m\sigma^2 = k_{\text{B}}T, \quad (3)$$

where  $m$  is the mass and  $k_{\text{B}}$  is Boltzmann's constant. Replacing  $\sigma$  with  $p$  in previous formula leads to the well-known Doppler width.

### 5.2. Velocity vector field

The local ion velocity can be assumed to correspond to either the mean or the most probable velocity. In the case of 2D-LIF measurements, one therefore obtains the transverse (radial) and longitudinal (axial) velocity components from which the ion velocity vector can be constructed. Here a cylindrical symmetry is assumed. This point is discussed in section 7. The velocity vector field was determined in the plume near-field for the 5 kW SPT140 thruster [38], for the 5 kW P5 thruster [25], for the 500 W Stanford HT [41] as well as for the 200 W BHT-200 [39] and 600 W BHT-600 [20] thrusters. Recently, Huang and co-workers have reconstructed the velocity vector inside the channel of the 6 kW-class H6 HT [42]. They showed that the vectors point toward the surface nearby walls. Their results have major implications for the channel wall erosion studies. The ion velocity vector field was also mapped by Spektor and co-workers in the plume of a low-power HT with a cylindrical discharge chamber [21]. This so-called cylindrical HT features a reduced surface-to-volume ratio and a specific cusp-type magnetic topology [43].

Figure 10 displays the Xe II ion velocity vector field near the channel exit plane of the BHT-200-X3 thruster operating at 250 V [37]. The ion velocity is here taken as the most probable velocity  $v_{\text{mp}}$ , i.e. the peak of the fluorescence line shape. The

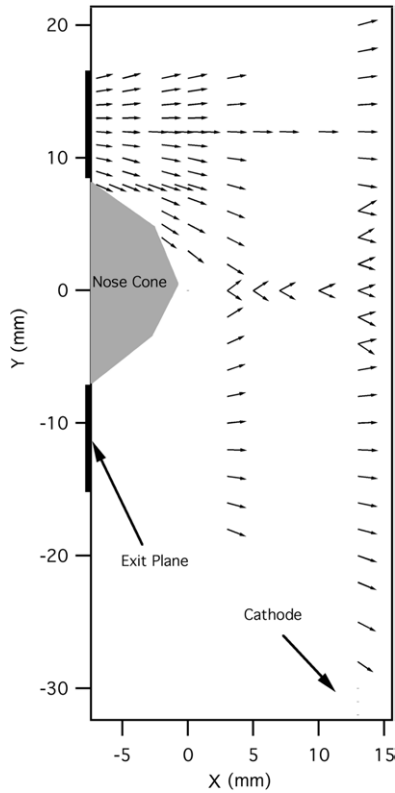


**Figure 10.** Velocity vector field near the exit plane of the BHT-200-X3 thruster firing at 250 V [37].

ions diverge as they emerge from the discharge channel but on the channel centerline, which is in fact a symmetry axis. The interaction between ion populations originating from the opposite side of the channel is well illustrated in figure 10. Mixing of divergent velocity groups begins behind the nose cone tip, but appears most noticeably near the cathode plane ( $x = 13$  mm). An interesting feature of the flow field, also observed with other HTs, is the appearance of a high axial velocity, low radial velocity ion population on the thruster centerline, see also figure 9. This region of broad radial velocity distribution centered around  $v_r = 0$  has tentatively been identified as a stationary ion-acoustic shock wave [40].

### 5.3. Velocity profile and accelerating potential

The evolution of the Xe II ion axial mean velocity  $\bar{v}_x$  along the channel axis of the 5 kW PPS®X000-ML thruster is displayed in figure 11 for a discharge voltage  $U_d$  ranging from 300 up to 700 V [17]. In figure 11, the dashed line corresponds to the ion velocity obtained assuming a full conversion of the potential energy  $eU_d$  into axial kinetic energy. The highest value of the mean ion axial velocity component is close to the theoretical limit but always stays below it. The supplied potential energy is in fact not fully converted into axial motion. First, a part contributes to the radial velocity, i.e. divergence of the ion beam. Second, voltage loss occurs during the ionization and acceleration process [4, 40]. This loss is composed of the anode and cathode voltage drops, the ionization loss, the electron loss, wall losses and the voltage drop between the beam and the cathode. The overall potential loss is typically a

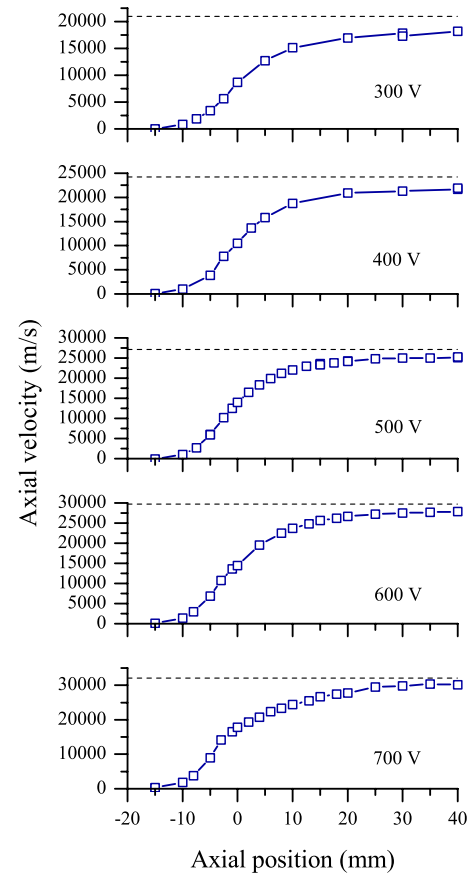


**Figure 11.** Xe II mean axial velocity along the channel axis of the PPS®X000-ML thruster for several discharge voltages [17].

few tens of volts. It tends to decrease with the applied voltage as can be seen in figure 11. The length of the acceleration layer is around 40 mm in this example. The breadth of the acceleration region in a HT is typically one channel mean radius. As can be seen in figure 11, the shape of the velocity profile depends on the applied voltage: the gradient is steeper when  $U_d$  is ramped up and the whole profile is shifted toward the anode. The shape of the on-axis ion velocity development also depends upon the magnetic field, the gas flow rate, the channel geometry, the propellant and the cathode-to-ground potential. The interested reader can find related information in, e.g., [17, 18, 23, 36] and references therein.

The accelerating potential  $U_{acc}$  is derived from an energy conservation equation:

$$\frac{1}{2}mv^2 = eU_{acc}, \quad (4)$$

where  $v$  is the ion velocity and  $e$  is the elementary charge. The ion velocity can be either  $\bar{v}$  or  $v_{mp}$  or any other definition. The accelerating potential profile along the channel axis of the PPS100-ML thruster is shown in figure 12. The potential was computed from the ion mean velocity. In this experiment the thruster was operated at 250 V and  $4.5 \text{ mg s}^{-1}$  xenon flow rate [44]. A large fraction of the ion acceleration occurs behind the channel exit plane. This is often the case for HTs, see, e.g., [17, 23, 36], although the outside fraction depends on the magnetic field map and on the thruster geometry. Figure 12

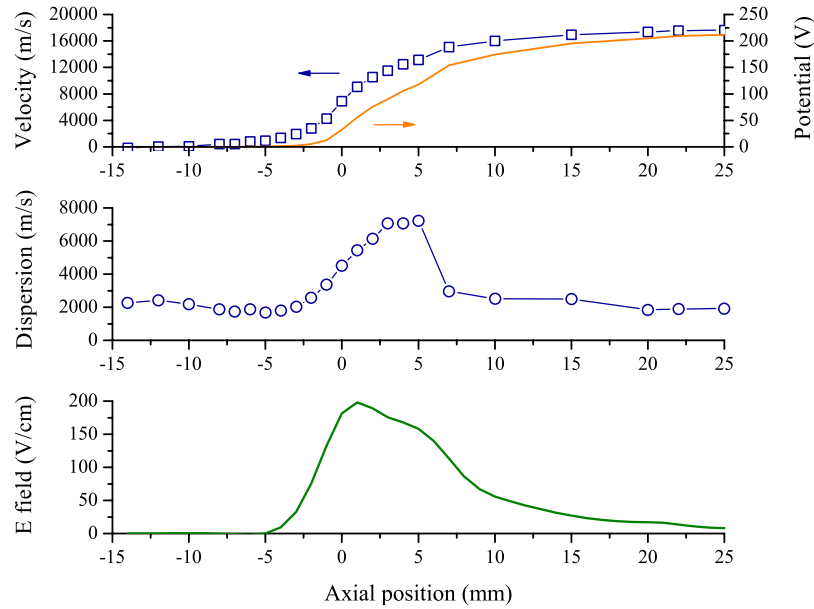


**Figure 12.**  $\text{Xe II}$  ion mean velocity, accelerating potential, velocity dispersion ( $p$  parameter) and electric field as a function of the  $x$  position for the PPS100-ML thruster operating at 250 V [44].  $x = 0$  indicates the channel exit plane.

also illustrates that acceleration occurs over a relatively short distance. At the end of the acceleration region the potential is 212 V for an applied voltage of 250 V. Such numbers reveal the high energy conversion efficiency, which is an intrinsic characteristic of a HT discharge.

#### 5.4. Interconnection between ionization and acceleration layers

As previously addressed in section 4.2, the ion VDF broadens in the course of the flow. The broadening effect along the  $x$  direction is clearly visible in figure 6. The evolution of the velocity dispersion  $p$  along the channel axis of the PPS100-ML thruster is shown in the middle panel of figure 12. The dispersion follows a single-peaked curve. The maximum value of  $p$ , which is around  $7000 \text{ m s}^{-1}$ , is reached in the vicinity of the thruster channel exit plane. The fact that the widest ion VDF is encountered at the channel exhaust is not related to the magnetic field distribution, although the latter may have a little influence. Moreover, as measurements are performed along the channel centerline, the divergence has no impact on the velocity dispersion. The large value of  $p$  originates from the interconnection between the ionization and the acceleration regions, as explained hereinafter. The distribution shown in figure 12 has a shape that is typical for a HT whatever the input power and size: the dispersion first increases slowly up to a maximum value; it then exhibits a sharp decay toward a constant level that is never zero. The magnitude of the velocity dispersion depends upon the thruster operating conditions, see, e.g., [17]. The velocity dispersion profile along the channel axis is the same with xenon and krypton, see, e.g., [23, 28] for measurements with krypton in low-power thrusters. An example of measurement outcomes with Kr as propellant is illustrated in figure 13. The velocity dispersion is expressed in terms of ion temperature by way of equation (3). Results were obtained near the exit plane of the PPI thruster operating

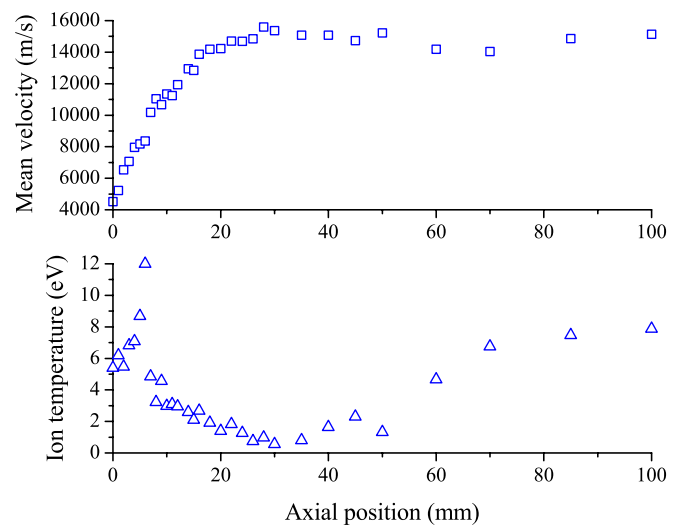


**Figure 13.** Mean velocity and ion temperature versus the  $x$  position (channel axis) for the PPI thruster operating with krypton [23].

at 200 V [23]. The corresponding  $\text{Kr II}$  ion VDFs are given in figure 7; yet only populations (1) and (2), which composed the main ion beam, are taken into account. As mentioned above, the ion temperature reaches a maximum before decreasing quickly to a non-zero value. However, in figure 13 the ion temperature increases again behind  $x = 40 \text{ mm}$ . This is a direct consequence of the interaction between elementary ion beams that diverge from the opposite sides of the channel. Consequently, the  $\text{Kr II}$  ion mean velocity profile exhibits a trough.

The broadening of the ion VDF in the course of the flow and the value of the velocity dispersion are at present well understood. They originate in the overlap between the ionization and the acceleration layers [17, 18]. The broadening of the ion VDF along the channel axis in the direction of the

flow is a general feature for HTs that depends neither on the size of the thruster nor on the operating conditions. Numerical simulations carried out with both hybrid and PIC models show that the ion VDF broadening phenomenon finds its origin in the existence of a partial overlap between the ionization layer and the acceleration layer. Calculations carried out with a hybrid model when the electron properties are frozen indicate that the on-axis distribution of the velocity dispersion depends strongly on both the shape and the position of the ion source term. These two parameters in fact determine the degree of overlap between the two zones. Oscillations of the accelerating potential can amplify the phenomenon when they lead to an increase in the length of the overlap region. CEX collisions between atoms and ions play a minor role in the value of  $\sigma$  or  $p$  as the mean free path length is far above the typical size of the acceleration layer. Computational simulations also indicate that the maximum of the velocity dispersion is reached at the end of the ionization layer, i.e. at the location where no more ions are produced at rest.

All studies reveal that a large fraction of ions are produced inside the acceleration region. The overlap between the production and acceleration regions is at the origin of a strong interrelation between the ionization and acceleration processes. In fact, this should not be too surprising as ionization and acceleration take place in the region of large magnetic field strength wherein the Hall current is large. As a consequence, the thrust level and the specific impulse of a single-stage HT cannot be tuned in an independent manner, which somewhat limits the versatility of such a propulsion device. The only way to reduce the degree of interrelation is to move to a more advanced two-stage thruster design for which the ionization and acceleration processes would be physically separated.

## 6. Electric field

### 6.1. Computation from the velocity profile

The electric field distribution is an important quantity for understanding the physics of a HT cross-field discharge. It can be either directly or indirectly inferred from the ion velocity measured by LIF spectroscopy. A first possibility is to derive the field from the macroscopic velocity  $\bar{v}$  or  $v_{mp}$ . For instance, the electric field in the axial direction  $E_x$  is the derivative of the acceleration potential distribution, the latter being directly linked to the velocity profile as we have seen. The  $E_x$  field therefore reads

$$|E_x(x)| = \frac{dU_{acc}(x)}{dx} = \frac{m}{e} v(x) \frac{dv(x)}{dx}, \quad (5)$$

where  $v$  can be either the mean or the most probable velocity. Note that in order to numerically compute  $E_x$ , it is often necessary to smooth the velocity profile and to interpolate the resulting curve using, e.g., cubic splines. The electric field distribution along the PPS100-ML thruster channel axis is shown in figure 12 together with the related velocity and potential profiles for  $U_d = 250$  V. The electric field profile is also shown in figure 14 for the PPS®X000-ML thruster firing

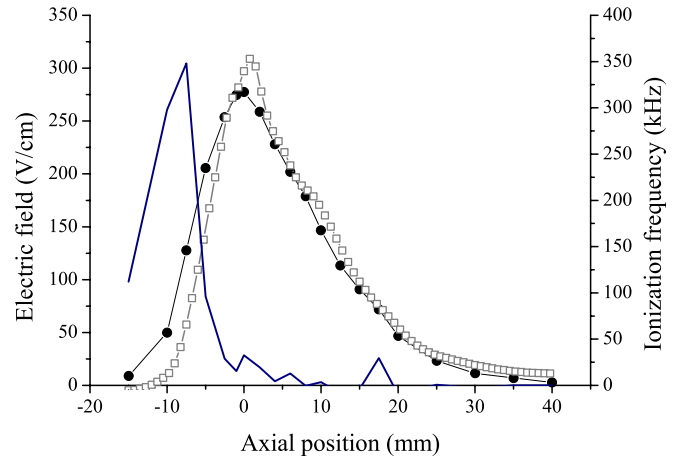


**Figure 14.** Development of the electric field along the channel axis of the PPS®X000-ML thruster at 600 V and  $6 \text{ mg s}^{-1}$ . Two approaches are compared: measurement of the Xe II ion mean velocity (square) and calculation of the ion VDF moments (circle) [17]. Also shown is the ionization frequency profile determined from the second method.

at 600 V. In both cases, the electric field has been calculated from the Xe II ion mean velocity profile. The properties of the  $E_x$  field are typical for HTs, see, e.g., [17, 18, 28, 32]. The largest magnitude of the field is around  $200\text{--}400 \text{ V cm}^{-1}$ . It demonstrates that a high electric field strength can be achieved in a magnetized discharge in cross-field configuration without the use of a grid assembly [2, 4], therefore avoiding space charge current limitation. The maximum is always near the channel exit plane, as the electric field profile is strongly connected with the magnetic field profile. The width of the distribution depends on the thruster sizes and a little on the operating conditions. It is roughly one channel mean radius.

### 6.2. Use of Boltzmann's equation

As a non-negligible number of ions are created within the acceleration layer (see the preceding section), the electric field computed from the mean or the most probable velocity profile is underestimated in the region where the two layers overlap due to local production of slow ions that have not yet experienced the potential drop. A powerful method, which relies on the use of Boltzmann's equation, has therefore been developed for evaluating the exact spatial profile of the electric field as well as the distribution of the ionization frequency directly from the measured ion VDF [45]. In their approach, Pérez-Luna *et al* established a relationship between the two quantities of interest and the moments of the measured 1D ion VDFs through Boltzmann's equation [45]. The key feature of this approach is that it properly accounts for collisions. Note that to obtain proper results, the experimental VDFs must be normalized taking into account the laser power, the detector response and the lock-in amplifier settings.

Calculation outcomes are illustrated in figure 14 for the PPS®X000-ML firing at 600 V. The electric field and the ionization frequency are plotted as a function of position along the channel axis. There is a large overlap between the electric field and the ionization profiles, which indicates that a part of

the ionization process occurs in the region of strong electric field, as previously discussed. Of course, the distribution of  $E_x$  computed from the VDF moments is not far from the one inferred from the mean axial velocity profile. However, as the ionization process is accounted for in the Boltzmann method, the effect of ions created at the beginning of the acceleration layer is withdrawn. Figure 14 clearly indicates that the electric field is underestimated in the ionization layer when the mean or the most probable velocity is used for the calculation.

The method based on the velocity moments of Boltzmann's equation was later extended to the 2D case by Spektor, see [46]. It is therefore possible to compute the real electric field vector distribution from 2D LIF measurements of both the axial and the radial ion velocity components. Applying the 2D method on a cylindrical HT plasma, Spektor was for example able to show the critical role of the pressure tensor on the 2D electric field computation in regions where densities are large [21, 46].

## 7. Ion azimuthal velocity

### 7.1. Ion fluid rotation

In the crossed-field discharge of a HT, ions are commonly assumed to be unmagnetized, in contrast to the electrons which are highly confined. In fact, the Larmor radius of ions reaches several tens of centimetres whereas it is  $\sim 1$  mm for electrons with a 200 G magnetic field. Therefore, electrons undergo a fast  $\mathbf{E} \times \mathbf{B}$  drift in the azimuthal direction, which forms the so-called Hall current. By contrast, ions never achieve a complete rotation along the channel circumference. However, under the influence of a  $v_{\text{axial}} \times \mathbf{B}$  Lorentz force, ions can be azimuthally deflected from a purely axial trajectory. This is a crucial point for the thruster operation since it can affect the thrust vector direction and apply a torque to the satellite.

The first attempt to measure the azimuthal velocity of Xe II ions was made by Manzella in 1994 with a 1.5 kW-class SPT-100 thruster [47]. The azimuthal velocity was found to be around  $250 \text{ m s}^{-1}$  and the torque was  $5 \times 10^{-3} \text{ N cm}$ . More recently, Hargus and co-workers used a LIF technique to study the evolution of the ion rotation velocity in a 600 W HT operating at 300 V [37]. An azimuthal velocity around  $500 \text{ m s}^{-1}$  was measured at the channel outlet. Interestingly, Hargus *et al* found a small gap in the ion azimuthal velocities between the two opposite sides of the channel, but the origin of the asymmetry was not discussed in their paper. The torque was estimated to be  $3 \times 10^{-3} \text{ N cm}$ , close to the value obtained by Manzella. As we shall see in the next two paragraphs, the ion fluid rotation in a HT plasma is in fact more complicated than expected: the azimuthal drift is asymmetrical and the velocity does not solely depend on the magnetic field.

### 7.2. Sign convention

A series of LIF measurements was recently performed with the 1 kW-class PPS100-ML HT to accurately investigate the change of the Xe II azimuthal velocity component with the magnetic field, the voltage and the gas flow rate [48]. Figure 15 sketches the thruster channel and the orientation of

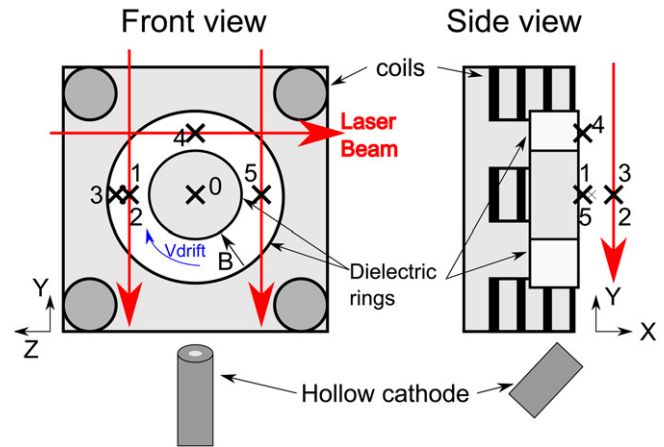


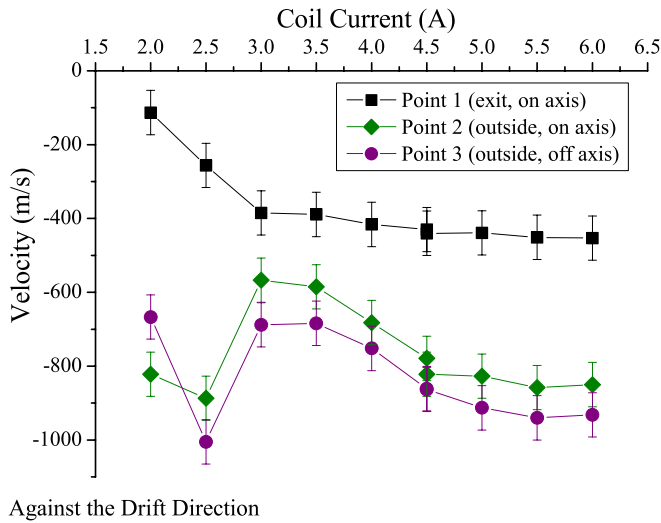
**Figure 15.** Front and side view diagrams of the HT and laser beam geometry for azimuthal velocity measurements [48]. Also shown is the drift direction ( $I_c > 0$ ). Coil current is positive, so plasma drift is clockwise when facing thruster exhaust plane. Numbers refer to measurement points.

the monitoring laser beams. The azimuthal velocity profiles were examined at five locations. Three of them are situated in the same ( $y, z$ ) plane close to the channel exit plane. They are all on the channel midpoint at various angles. The other two are situated downstream on the same channel side along a horizontal line that crosses the thruster axis as shown in figure 15. For all measurement points, the laser beam wave vector is such that only the azimuthal component of the velocity can be detected.

With the LIF technique, the acquired quantity is the velocity component along the propagation direction of the laser beam, see section 3.1. Hence the Doppler shift can be either positive or negative. To get a clear idea of the direction of the ion azimuthal velocity, a rule that depends neither on the laser beam direction nor on the magnetic field direction is preferred. The sign of the azimuthal velocity is then chosen with respect to the direction of rotation of ions due to the Lorentz force  $v_{\text{axial}} \times \mathbf{B}$ . Note that the Lorentz force direction is similar to the electron  $\mathbf{E} \times \mathbf{B}$  drift direction. If ion azimuthal velocity is only driven by the magnetic deflection, its sign according to our convention is always positive, i.e. in the direction of the Lorentz force. Then, any change in velocity sign indicates that another mechanism is acting on the ion trajectory. In the next section, an azimuthal velocity along the Lorentz force is said to be positive and referred to as 'along the drift'. In contrast, a velocity in the opposite direction is counted negative and referred to as 'against the drift'.

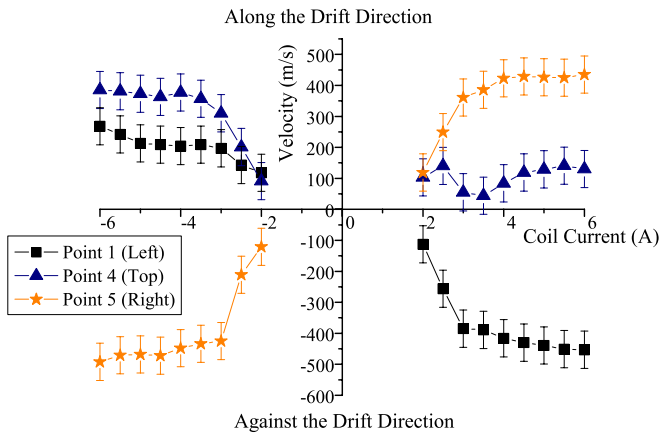
### 7.3. Impact of the magnetic field

The evolution of the Xe II ion azimuthal velocity  $v_\theta$  with the magnetic field intensity and orientation was investigated while keeping the discharge voltage and the mass flow rate constant:  $U_d = 200 \text{ V}$  and  $\Phi_a = 3 \text{ mg s}^{-1}$ . The graph in figure 16 displays  $v_\theta$  against the coil current  $I_c$  for three locations on the left side of the PPS100-ML HT [48]. Surprisingly, all velocities are negative, i.e. against the drift direction. Moreover, in all cases the velocity magnitude is much larger than the value calculated from the magnetic deflection [48].



Against the Drift Direction

**Figure 16.** Ion azimuthal velocity versus coil current for three locations on the thruster left side [48].



Along the Drift Direction

Against the Drift Direction

**Figure 17.** Evolution of the ion azimuthal velocity with coil current for the points near the channel outlet [48].

This suggests a force is acting on the ions to direct their velocity from the thruster top to bottom. To get more insight into the origin of the  $Xe^{II}$  azimuthal path, the magnetic field direction was changed by inverting the coil current. Hence, only the direction of the Lorentz force is modified with this operation. The azimuthal velocity is plotted in figure 17 as a function of the coil current, with both positive and negative values, for observation points 1, 4 and 5. As shown in figure 17, for two of the six measurement series, the velocity is in the direction opposite to the plasma drift. For these two cases—point 1 with  $I_c > 0$  and point 5 with  $I_c < 0$ —the Lorentz force is oriented in the upward direction. We should point out that, except for point 4 with  $I_c > 0$ , the modulus of the azimuthal velocity is much larger than the calculated values. It finally comes out that for the side observation points 1, 2, 3 and 5, whatever the magnetic field direction, the main transverse force acting on ions is from the top to the bottom of the thruster.

#### 7.4. Role of the cathode

In the study by Bourgeois *et al.*, the influence of the discharge voltage and the gas flow rate on the ion azimuthal drift

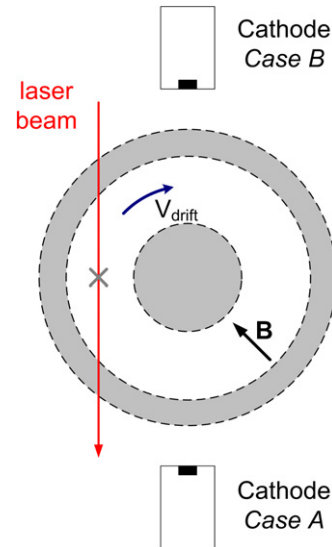


**Figure 18.** Configuration for ion drift examination with the permanent magnet PPI thruster. The cross indicates the measurement point.

was also examined [48]. All results support the idea of an additional phenomenon superimposed to the magnetic deflection. The additional force applied on ions can be attributed to the asymmetry of the plasma due to the position of the cathode. The latter is located below the thruster body, just beyond the channel exit plane. Ions leaving the channel are certainly attracted toward the cathode and gain velocity in the direction orthogonal to the main acceleration direction. A weak transverse electric field directed toward the external cathode could considerably influence the trajectory of the ions, whose azimuthal velocity would no longer only be driven by magnetic deflection. The cathode attraction force would be particularly dominant when the measurement location was at a right angle with respect to the cathode axis, as is the case for points 1 and 5.

In order to investigate more deeply the role of the cathode on the ion azimuthal drift, a series of experiments has recently been carried out by our team with the low-power permanent magnet PPI thruster [49]. In one of them, the  $Xe^{II}$  ion azimuthal velocity has been measured at one fixed position (channel midpoint, exit plane) while changing the cathode location from bottom to top as depicted in figure 18. The results are displayed in figure 19 for several applied voltages. Case A is similar to case (1) in figure 16. However, here the velocity is positive, which means along the drift direction. This difference supports the idea that magnetic deflection is not the main mechanism at the origin of the ion azimuthal velocity. The external cathode has a strong impact on the symmetry of the plasma, as can be seen in figure 19. The two velocities are positive, which is not in agreement with the picture of a transverse electric field toward the cathode. The azimuthal velocity increases, as well as the gap between cases A and B, with the applied voltage. The magnitude of  $v_\theta$  is well above the value calculated from a mere Lorentz force. Moreover, it seems that  $v_\theta$  increases with the thruster size, as noticed by Hargus and Charles [37]. Experimental outcomes indicate that the cathode

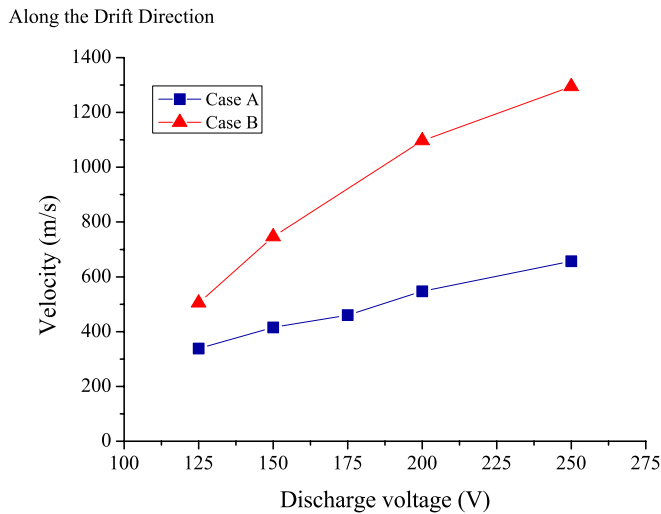


**Figure 19.** Azimuthal velocity versus applied voltage for two cathode positions [49], see figure 18.

plays a role in the ion azimuthal drift; however, a satisfactory model for explaining the properties of  $v_\theta$  is still to be discovered.

## 8. Atomic flow

### 8.1. Why probe atoms in HTs?

As we have seen, ion production along with ion acceleration governs thrust level, performance and lifetime in a HT. That is the reason why many experimental works have been devoted to characterization of the ion VDF by laser spectroscopy over the past decade. In contrast, little effort has been made to examine the atom transport phenomena. Although indirect, it is an interesting approach to gather complementary information about the ionization region and to better grasp the role of charge-exchange collision events and plasma-wall interactions on HT behavior and dynamics. It is also a powerful way of testing and validating various physical models of the  $\mathbf{E} \times \mathbf{B}$  discharge of a HT.

The first study on neutral xenon velocity in a HT was carried out in 1997 by Cedolin *et al* [50] with a low-power device. They observed a peak in the axial velocity component downstream of the channel exit plane. A few years later, Hargus and Cappelli conducted atom velocity measurements both in the interior and exterior parts of a HT channel for various applied voltages [19, 41]. They confirmed that neutrals are accelerated within the thruster whatever the operating conditions. As an explanation, they proposed depletion of the lowest atomic velocity classes due to ionization. In a recent work, Huang and Gallimore examined the axial velocity profiles of xenon atoms in a high-power HT [51]. The axial velocity distribution revealed that the atom flow accelerates up to the thruster exhaust and decelerates outside it. They also investigated the possible impact of charge-exchange collisions between neutrals and ions. In a recent paper, our team performed LIF measurements on short-lived and long-lived excited Xe atoms within the channel and the near-field plume of the 1 kW-class PPS100-ML HT [27]. By comparing numerical

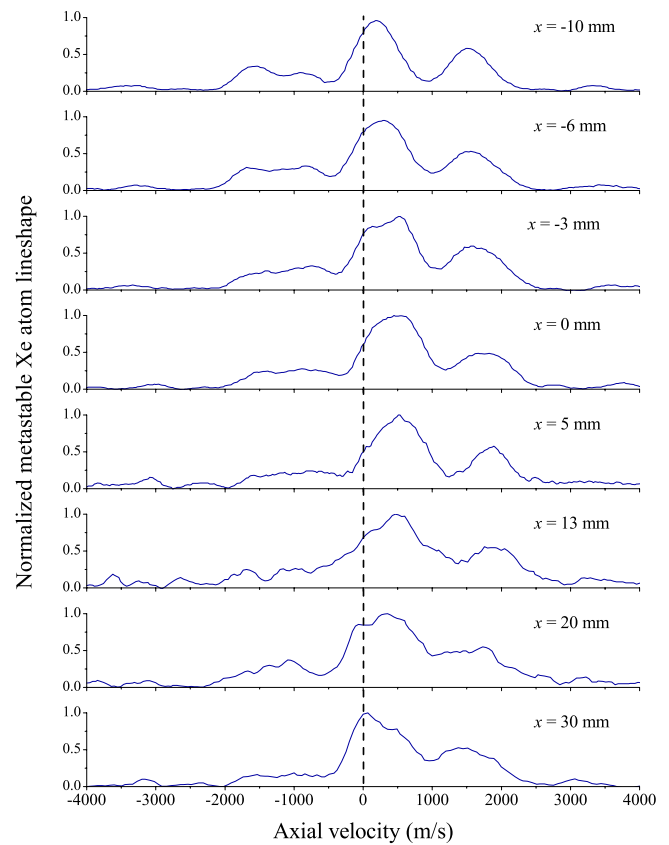


**Figure 20.** Series of line profiles of the 823.2 nm line connected with the Xe  $1s_5$  level [27]. Measurements were taken on the PPS100-ML channel axis (250 V);  $x = 0$  refers to the channel exit plane.

outcomes of a kinetic/fluid hybrid modeling with experimental results, it was possible to fully explain the shape of the atom velocity profile.

### 8.2. Atomic line shape

The density of Xe atoms in the resonant  $1s_2$  state is low due to its short lifetime. As a consequence, the fluorescence signal is lost behind the thruster channel exit plane, which means the atom behavior can solely be interrogated inside the channel with the 834.7 nm line. By contrast, a large atomic population is stored in the long-lived  $1s_5$  state. The 823.2 nm radiation can then be captured downstream of the channel exhaust. Moreover, the long lifetime of Xe( $1s_5$ ) atoms under HT plasma conditions ensures they behave similarly to ground-state Xe atoms.

A series of line shapes that correspond to the  $1s_5 \rightarrow 2p_5$  transition at 823.2 nm is displayed in figure 20. Spectra were recorded at several axial positions along the channel axis of the PPS100-ML HT fired at  $U_d = 250$  V. The complicated structure of the line originates from the existence of numerous xenon isotopes. As can be seen in figure 20, the line center, which corresponds to the atom's most probable velocity, shifts toward large velocity values all the way to the exit plane ( $x = 0$ ). Behind the outlet, the peak shifts in the opposite direction. Note that the Doppler shift always stays positive. Moreover, the line broadens in the course of the flow.

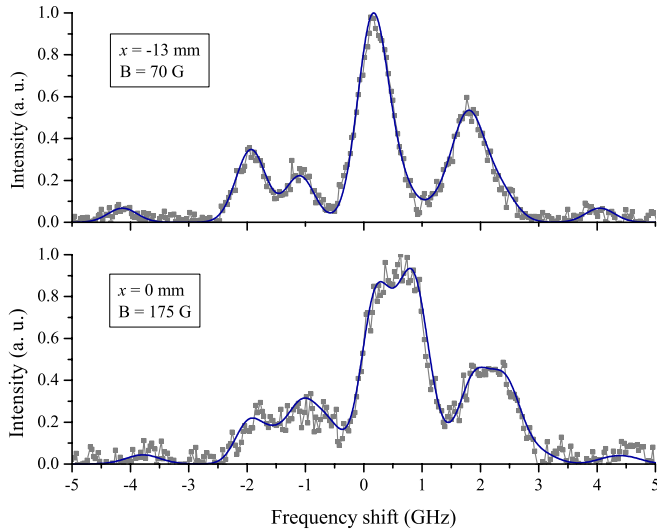


**Figure 21.** Experimental (squares) and computed (line) lineshape for the 823.2 nm transition at two locations along the PPS100-ML channel axis (250 V) [27].

### 8.3. Line shape modeling

For the two xenon atom excited states, see section 3.3, the most probable velocity is given by the Doppler shift of the line center. In order to extract a larger amount of information from the measured spectra, the line profile has to be reconstructed taking into account the isotopic and hyperfine structures, Zeeman splitting [30], Doppler broadening and the power saturation effect. More information about the modeling procedure can be found in [27]. For the interested reader, additional information about the deconvolution of fluorescence spectra can be found in [30, 52, 53].

To illustrate the modeling outcome, in figure 21 computed line profiles are superimposed to experimental spectra obtained at  $x = -13$  and  $x = 0$  mm when the PPS100-ML thruster operates at 250 V. In the two cases, the gas temperature is fixed at 700 K. The gas is assumed here to be in thermal equilibrium with the channel walls. The Xe atom mean velocity is then obtained by fitting a calculated spectrum to the data points. The agreement between experimental and computed line shape is satisfactory, as illustrated in figure 21. This approach allows one to extract fluid quantities with reasonable accuracy. As we will see in the next section, it is necessary to account for two atom populations outside the channel to reliably reproduce the measured line shapes, which makes the fitting procedure more complicated.

### 8.4. Accelerating and decelerating flow

The evolution of the Xe atom axial velocity component along the channel axis is displayed in figure 22 for various thrusters and operating conditions: PPS100-ML [27], PPS®X000-ML and Stanford HT [41, 50]. The Xe  $1s_1$  velocity corresponds to the peak of the measured line profile but for the  $1s_5$  metastable state in the PPS100-ML. In that case the mean velocity arises from a model of the measured line shape with a gas temperature fixed at 700 K. As can be seen in figure 22, all experimental profiles give the same tendency. The atom velocity increases inside

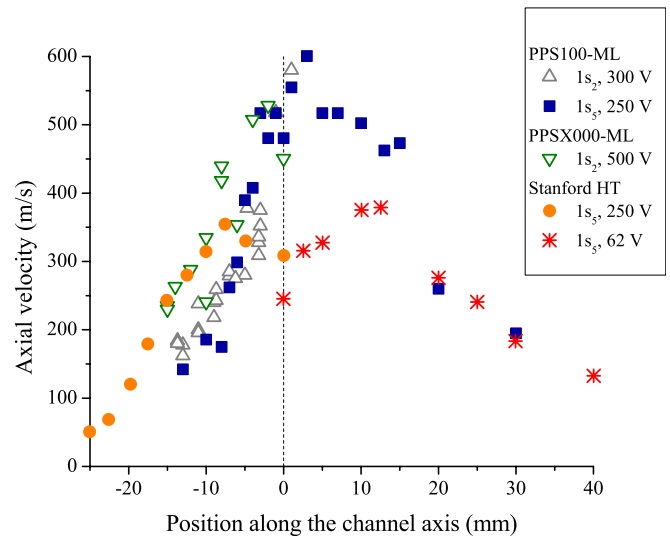


**Figure 22.** Axial velocity profiles of Xe ( $1s_2$ ) and Xe ( $1s_5$ ) atoms for various HTs. The position  $x = 0$  indicates the channel exit plane.

the channel. The maximum axial velocity, whose value seems to depend on the thruster design, is reached near the channel exit plane. Behind the exhaust, the velocity declines gradually toward zero. Two mechanisms can readily be identified to explain the apparent acceleration of the atomic gas in the interior of the thruster. First, a symmetry break in the velocity space results from the fact that the channel is open on one side. This free-flow effect makes the negative component of the axial velocity weaker and weaker when moving toward the exit plane. As a direct consequence, the peak of the atom VDF shifts toward the positive values. Second, the ionization of slow atoms in the region of large electron density is highly probable owing to their relatively long residence time. Selective ionization is then responsible for the loss of the slow wing of the atom VDF, hence a shift of the mean velocity to the high velocity side. As will be shown in the next section, although the proposed physical mechanisms allow one to explain the observed tendency, they are, however, not sufficient to explain the measured atomic velocity amplitude.

As can be noticed in figure 22, Xe atoms slow down behind the thruster exhaust. Since no force is acting on the atoms, beyond the channel exit plane one expects that they form a jet moving with a constant axial speed. The deceleration of the atom flow is actually due to invasion of the jet by atoms that originate both from the hollow cathode and from the background gas. Some of these atoms are locally brought into an excited state by electron impact. The atom VDF therefore exhibits two components: a fast and hot component that corresponds to atoms from the jet as well as a slow and cold component that comprises atoms from the cathode and the residual gas. This view is supported by the fact that theoretical line shapes do not conform to experimental spectra when solely considering one group of Xe atoms [27]. The axial velocity of the two atoms populations is shown in figure 23. Measurements have been realized on the  $1s_5$  metastable level with the low-power PPI thruster operating at 200 V [49]. The velocity was extracted using a model of the line shape. The invasion of the discharge by slow and cold atoms is clearly identified here.

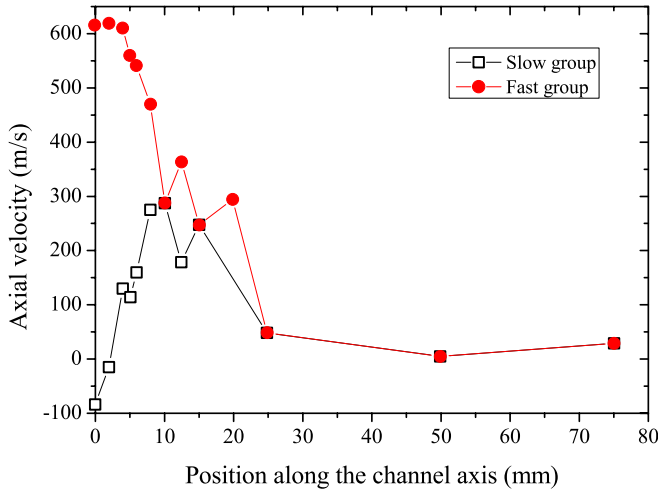


**Figure 23.** Slow and fast atom population behind the channel exit of the PPI thruster firing at 200 V [49]. LIF measurements on the Xe ( $1s_5$ ) level.

### 8.5. Influence of ion recombination at walls

The time-averaged Xe atom VDF was computed along the line of sight for a PPS100 thruster firing at 250 V by means of a hybrid model [27]. Several cases were investigated, varying the residual pressure level, the CEX collisions and the value of accommodation coefficient  $\alpha_w$  for ion–wall collisions. For all cases, the mean axial velocity was determined from the first-order moment of the simulated atomic VDF.

First, simulations were carried out neglecting the residual gas pressure with  $\alpha_w$  fixed to one, i.e. all Xe atoms were in thermal equilibrium with thruster walls after a collision event. Results indicate ionization and free-flow effects are not sufficient to explain the neutral flow acceleration in the interior of the thruster [27]. When CEX collisions are not included in the model, the axial velocity reaches a constant magnitude around  $470 \text{ m s}^{-1}$ . This value corresponds to the full conversion of thermal energy accumulated inside the channel into kinetic energy. With CEX collisions, the mean velocity increases steadily in the course of the flow. Numerical outcomes show that in spite of a low probability CEX collisions markedly influence the atom VDF.

Second, the background pressure was taken into account in the simulations with  $p_{\text{back}} = 2 \text{ mPa}$ . The residual pressure has a drastic impact upon the Xe atom velocity as can be seen in figure 24 for, e.g., the case  $\alpha_w = 1$ . This time the axial velocity decreases down to a low value around  $100 \text{ m s}^{-1}$  behind the channel exit plane. As previously stated, deceleration of the atomic flow is due to mixing between hot and fast atoms leaving the channel and slow and cold atoms from the residual gas. The simulated atom VDF was indeed made of two distinct components, see [27]. Although the shape of the velocity profile is well reproduced with the hybrid model when  $p_{\text{back}}$  and CEX collisions are incorporated, the calculated velocity magnitude is still in disagreement with the measured one, especially at the channel exhaust.

In the third case, the value of the accommodation coefficient  $\alpha_w$  was changed [27]. The impact of Xe II ions

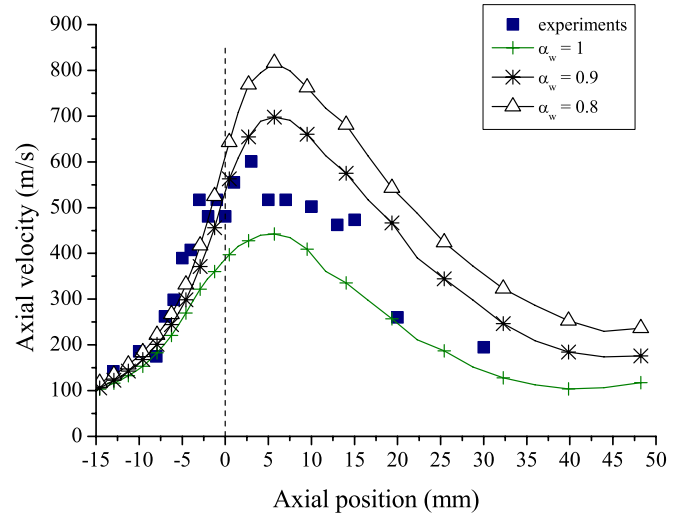


**Figure 24.** Simulated profile of the Xe atom mean velocity with  $p_{\text{back}} = 2 \text{ mPa}$  for three values of  $\alpha_w$  [27]. CEX collisions are included. Squares correspond to Xe ( $1s_5$ ) atom velocity measured with the PPS100-ML, see figure 22.

on channel walls of the HT leads to the creation of a non-negligible fraction of fast atoms when  $\alpha_w \neq 0$ . The creation of fast atoms naturally occurs in the final section of the channel, a region where the ion energy and the ion flux to the walls are large. Curves in figure 24 show that the acceleration of the atom flow is reasonably reproduced when  $\alpha_w = 0.9$ . Simulations therefore indicate that the observed rise in the Xe atom velocity results not only from ionization and flow expansion but also from creation of fast atoms at the walls due to recombination of ions.

## 9. Time-resolved LIF measurements

### 9.1. Motivations

It is well-established that the cross-field discharge of a HT is strongly non-stationary [4, 54]. This specific type of magnetized plasma displays numerous types of oscillations, which encompass many kinds of physical phenomena, each with its own length and time scales [54]. Current and plasma fluctuations, whose frequency range stretches from  $\sim 1 \text{ kHz}$  up to  $\sim 1 \text{ GHz}$ , play a major role in ionization, particle diffusion and acceleration processes. Low-frequency plasma oscillations in the range 10–30 kHz, so-called breathing oscillations, are especially of interest as they carry a large part of the power. Breathing oscillations find their origin in a prey–predator type mechanism between atoms and ions as shown by Boeuf and Garrigues [55]. In short, these oscillations originate in a periodic depletion and replenishment of the neutrals near the exhaust of the thruster channel due to the efficient ionization of the gas. The frequency is then linked to the time it takes for atoms to fill in the ionization region. With an atom thermal speed of  $300 \text{ m s}^{-1}$  and a region size of 20 mm, one finds a frequency of 15 kHz. The breathing phenomenon not only disturbs the discharge current but also has a strong impact on several quantities such as the ion beam divergence and energy and the electron density and temperature. Oscillations of the

mentioned quantities are most likely connected with a time variation of the potential distribution or, in other words, with the variation with time of the accelerating electric field. Therefore, it appears of considerable interest to investigate the temporal behavior of the electric field that certainly hides a rich and intricate dynamics. As the medium is collisionless within the acceleration layer, oscillations of the electric field can be assessed from the time-varying ion velocity with an appropriate numerical method.

As we have seen in section 3.2, a phase sensitive detection method is often used to capture the fluorescence signal in case of time-averaged LIF measurements. However, this method, which is powerful enough for the extraction of a signal in an environment with a high background noise level, offers a poor time resolution. To achieve the measurement of the time-resolved ion VDF in the plasma of a HT, it is necessary to develop a method able to detect LIF photons with a time resolution around  $1\mu\text{s}$ . Under normal operating conditions, the number of fluorescence photons observed at 541.9 nm with a continuous laser beam tuned at 834.72 nm with about  $1\text{ mW mm}^{-2}$  power density is on the order of  $10^{-2}$  per microsecond. Under identical experimental conditions, the number of background photons generated by the plasma at 541.9 nm during  $1\mu\text{s}$  is typically 1, which means a ratio of 100 between the two signal amplitudes. The laser system must therefore be able (i) to detect a tiny amount of photons hidden in a strong background and (ii) to determine with high accuracy the exact moment in time fluorescence photons have been produced. One must therefore turn to a photon-counting technique.

### 9.2. Photon-counting technique

To carry out time-resolved LIF measurements of the ion or atom VDF in the discharge and plume of a HT the optical assembly is similar to the one described in section 3.2. Only the fluorescence radiation detection system is modified: the lock-in detector is replaced by a pulse counter. The photon, or pulse, counting technique allows the detection of a very low level signal with an excellent time resolution. When combined with a modulation of the laser light intensity, the counting technique can distinguish between LIF photons and spontaneous emission photons [57]. Here we briefly outline the main characteristics and settings of the system we have developed (see [44, 56] for more details). Photons are detected by means of a high gain and low dark noise PMT. A fast amplifier/discriminator module is used to screen out PMT dark current to limit the pulse rate, thereby avoiding saturation of the counter, and to transform any single event—here the arrival of a photon—into a TTL pulse. Pulses are subsequently treated by the pulse counter device, which counts events as a function of time. Our most recent system is based on a multichannel scaler MCS-pci<sup>®</sup> from Ortec. A trigger starts the counter which segments photon count data into sequential time bins. The instrument records the number of photons that arrive in each bin. In order to considerably improve the signal-to-noise ratio, the counter is able to operate in real-time addition–subtraction mode. The laser beam intensity

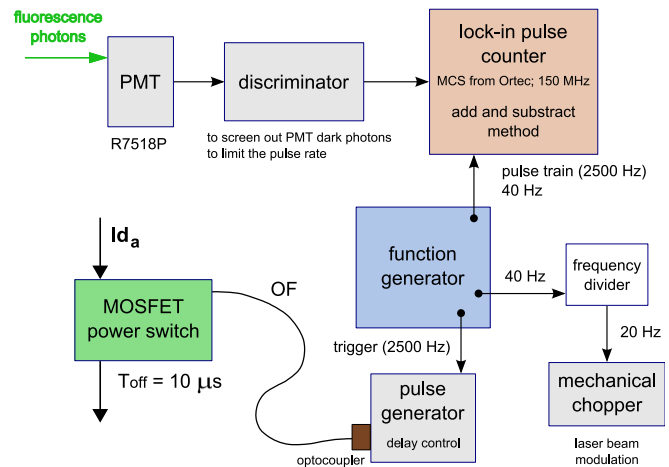


**Figure 25.** Block diagram of the pulse counting system [44, 56]. The discharge current switch is externally driven by the counter.

is modulated at  $\sim 20\text{ Hz}$  by means of a mechanical chopper. Each pulse recorded when the laser is propagating through the plasma is added to the time series. Each pulse recorded when the laser is suspended is subtracted from the time series. A function generator delivers a 2.5 kHz signal that at the same time controls the  $10\mu\text{s}$  long discharge current break and triggers the acquisition chain. In addition to providing a reference time, current interruption allows us to stabilize the discharge in a quasi-periodic regime, which is crucial for our measurements as data acquisition is a cumulative process. A block diagram of the counting device is displayed in figure 25. The time resolution, i.e. the width of each bin, was set to 100 ns and 4000 bins were used. The duration of one measurement cycle is therefore  $400\mu\text{s}$ , corresponding to about 8 times the period of low-frequency current oscillations. To obtain a reasonable signal-to-noise ratio, light was accumulated over 1 million cycles. The procedure to obtain the time-dependent ion VDF at a given position consists in accumulating photons in time at a fixed wavelength, i.e. in recording the time evolution of a well-defined ion velocity group [44, 56]. At least 12 different wavelengths are needed to create a reliable VDF.

### 9.3. Time evolution of the ion VDF

Time-resolved LIF measurements have been carried out in the discharge of the PPS100-ML HT at 250 V and  $4.5\text{ mg s}^{-1}$  [44]. Metastable  $\text{Xe II}$  ions were excited at 834.72 nm. As previously mentioned, the ion flow dynamics was investigated after a fast shut-down of the anode discharge current. It was therefore possible to examine the temporal characteristics of the ion VDF during forced and free low-frequency discharge oscillations. The interested reader can find more information about the experimental procedure, the acquisition of the fluorescence signal time series and the spatio-temporal dynamics of the various ion velocity groups in [44, 58].

Figure 26 shows contour plots of the time evolution of the  $\text{Xe II}$  ion axial VDFs for two positions along the thruster channel axis. In figure 26, ions with a relatively low velocity, but above the thermal speed that is around  $310\text{ m s}^{-1}$ , are

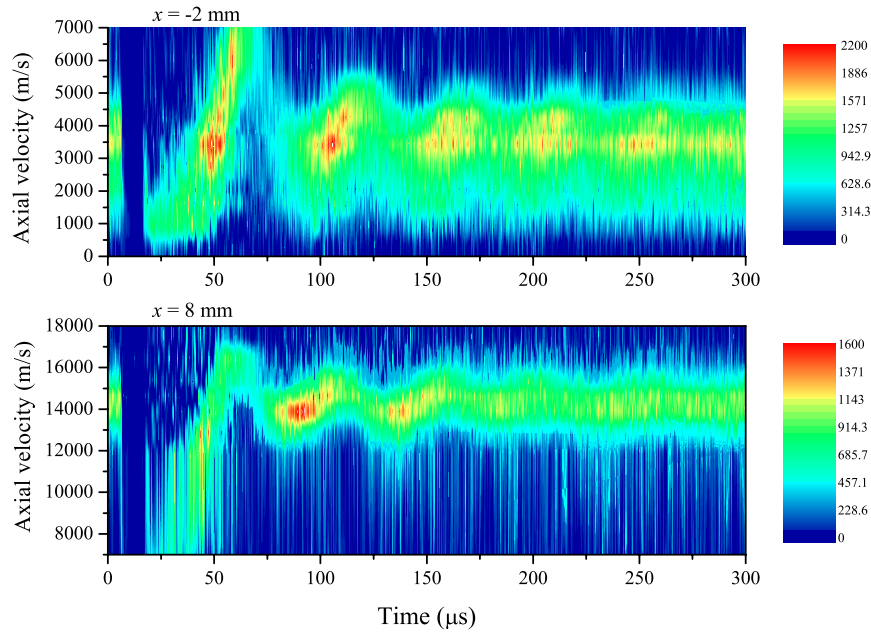


**Figure 26.** Contour plot of the Xe II ion axial VDF as a function of time for two locations along the channel axis of the PPS100-ML thruster [44]. The colorbar indicates the number of counts.

produced everywhere at re-ignition. At  $x = -2$  mm, ions flow immediately at about  $1000 \text{ m s}^{-1}$ . Although electrostatic acceleration is not an instantaneous process, a weak electric field is enough to bring ions to high velocity in a short period of time. For instance, starting from a null velocity, ions reach  $2200 \text{ m s}^{-1}$  in  $1 \mu\text{s}$  when experiencing a  $30 \text{ V cm}^{-1}$  field. This value roughly corresponds to a linear distribution of the 250 V anode-to-cathode potential. Despite being low, the ion velocity after discharge re-ignition is not the same everywhere, being higher outside the channel. This indicates that the electric field is established on a time scale shorter than the period of the breathing oscillations with an amplitude larger behind the exit plane. The quick rise of the ion velocity right after discharge re-ignition is followed by a gradual increase in the velocity during about  $50 \mu\text{s}$  until the latter reaches a limit whose value depends on the location. Subsequently, the ion VDF varies in time with a period of about  $50 \mu\text{s}$ , especially during the first free plasma oscillations. This phenomenon indicates that the acceleration potential, and thus the electric field, is likely to oscillate in time with a frequency on the order of the main discharge current oscillation frequency.

#### 9.4. Low-frequency oscillations of the electric field

Since heavy particle collision events are scarce in a HT discharge, ion acceleration is purely electrostatic and the electric field can be extracted from the relationship between the ion kinetic energy and the accelerating potential, see section 6. However, this approach is only valid either in steady state or when exploring a span of time much longer than the plasma breathing oscillation time [58]. One must therefore turn toward a more sophisticated way to compute the temporal characteristics of the electric field.

An appropriate method consists in using a Lagrangian description of the ion fluid motion. The electric field can then

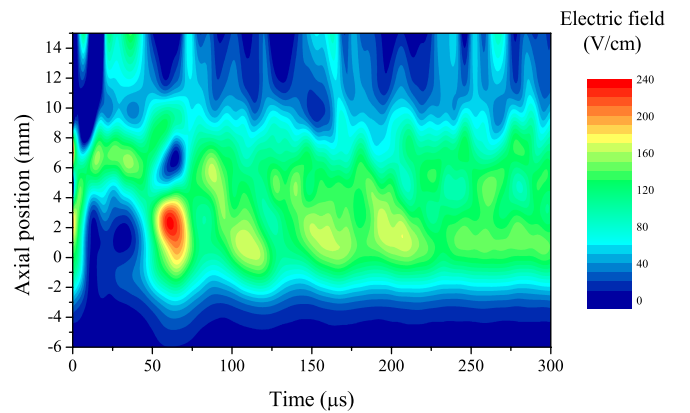


**Figure 27.** Spatio-temporal characteristics of the axial electric field computed from a Lagrangian description of the ion fluid motion. [44].

be computed from the material derivative of the ion velocity, i.e. the derivative taken along a path moving with velocity  $\mathbf{v}$ . From the equation of motion for unmagnetized ions, the axial component of the electric field  $E_x$  reads [49]:

$$E_x = \frac{m}{e} \left( \frac{\partial \bar{v}_x}{\partial t} + \bar{v}_x \cdot \frac{\partial \bar{v}_x}{\partial x} \right), \quad (6)$$

where  $\bar{v}_x$  is the mean Xe II ion axial velocity in the  $x$  direction. Note that equation (6) can be obtained from the ion momentum conservation equation for an incompressible fluid assuming a collisionless medium as well as steady and uniform particle density [49]. The evolution of  $E_x$  in space and in time is given in figure 27. As expected from the time evolution of the mean velocity, the electric field oscillates with a time period of  $\sim 50 \mu\text{s}$ . Disregarding the strong amplitude jump that follows the discharge current ignition, the amplitude change is of about  $40 \text{ V cm}^{-1}$  right behind the channel exit

plane. The electric field is mostly localized within a region that stretches from  $x = -2$  to  $x = 8$  mm, in agreement with time-averaged data, see [44]. From the contour plot in figure 27, one remarks that the electric field not only oscillates through time but also exhibits changes in space. During one oscillation of the discharge current, an electric field front seems to propagate toward the interior of the channel at low velocity. For the first forced oscillation, the front velocity is around  $700 \text{ m s}^{-1}$  whereas for all other oscillations the velocity is  $\sim 250 \text{ m s}^{-1}$ . The velocity is close to the xenon atom thermal speed. Therefore, the electric field, or in other words the acceleration layer, would move with the ionization layer as a direct consequence of the prey–predator process at the origin of the Hall discharge breathing oscillation. This is expected as the ion velocity dispersion stays almost unchanged in time [44, 58].

Although experimental results show that near the thruster exit plane an electric field front propagates upstream periodically, the observed phenomenon could be artificially amplified or distorted as no momentum source term is taken into account when computing  $E(t, x)$  using equation (6). However, Bourgeois has recently shown that the electron pressure gradient and the ionization term in the momentum equation can be neglected in comparison with the velocity material derivative and the electric term, respectively [49]. The spatio-temporal electric field dynamics illustrated in figure 27 is therefore exact. It can then be used as a test case for validation of advanced modeling of a HT discharge. An open question nevertheless remains: how exactly does the electric field front propagate in time? As time-resolved LIF measurements have only been performed at one position along the channel radius, one cannot distinguish between a pure axial motion and a helicoidal motion.

## 10. Conclusions and prospects

This article gives a review of recent investigations of the magnetized plasma of a HT by means of time-averaged as well as time-resolved laser-induced fluorescence spectroscopy. The  $\text{Xe I}$  and  $\text{Kr I}$  atom and  $\text{Xe II}$  and  $\text{Kr II}$  ion velocity distribution function has been obtained after laser excitation of excited levels in the discharge chamber and near-field plume for a broad range of thruster power and size. The VDF allows one to assess important quantities such as the mean velocity, the temperature, the velocity vector and the electric field. As shown throughout the review, investigation of atomic and ionic transport phenomena is a powerful method for getting insights into the physical mechanisms at play in this specific electric propulsion device.

Although progress has been made over the past decade in the physics of HTs by way of LIF experiments, several aspects of the technology remain unclear, not to say obscure. That is the reason why many studies still have to be carried out. To close this review, we propose a non-exhaustive list of possible works for the near future. The unconfirmed formation of a stationary electrostatic shock wave on the thruster axis, where elementary ion beams merge, must be investigated. If it exists, its role in the ion beam divergence should be

clarified. So far, only singly charged ions have been observed. LIF measurements on multiply charged ion species, especially  $\text{Xe III}$  ions, would certainly bring relevant information about the ionization process. The impact of the thruster design on the VDF has not been examined enough; comparison between diverging cusped-field thrusters, cylindrical HTs and standard HTs is certainly a promising direction to follow. In order to gain knowledge of the anomalous electron diffusion across the magnetic barrier, a thorough comparison between experimental VDFs and numerical VDFs is required. Finally, considerably effort must be put into time-resolved LIF measurements. Not only must the propagation of an electric field front at the breathing mode frequency be investigated in a deeper way, the time-evolution of the ion VDF must also be studied at higher frequencies, especially in the so-called ion transit time regime, and for different thruster power levels.

## Acknowledgments

A large part of this work was carried out within the frame of the CNRS/CNES/SNECMA/Universités joint research program 3161 entitled *Propulsion par plasma dans l'espace*. The author wishes to thank Dr N Sadeghi for fruitful discussions and collaborations. A large part of this work would not have been accomplished without the contribution of D Gawron, G Bourgeois, K Dannenmayer, A Lejeune, L Garrigues and E Pawelec.

## References

- [1] Turner M J L 2009 *Rocket and Spacecraft Propulsion* (Chichester: Springer Praxis)
- [2] Jahn R G and Choueiri Y 2002 Electric propulsion *Encyclopedia of Physical Science and Technology* vol 5, 3rd edn (San Diego, CA: Academic) pp 125–41
- [3] Jahn R G 1996 *Physics of Electric Propulsion* (New York: Dover)
- [4] Zhurin V V, Kaufmann H R and Robinson R S 1999 Physics of Closed Drift Thrusters *Plasma Sources Sci. Technol.* **8** R1–20
- [5] Pottinger S, Lappas V, Charles C and Boswell R 2011 Performance characterization of a helicon double layer thruster using direct thrust measurements *J. Phys. D: Appl. Phys.* **44** 235201
- [6] Chang Diaz F R *et al* 2004 The VASIMR engine: project status and recent accomplishments *Proc. 42nd AIAA Aerospace Science Meeting (Reno, NV)* AIAA paper 04-0149
- [7] Aanesland A, Mazouffre S and Chabert P 2011 PEGASES—a new promising electric propulsion concept *EuroPhys. News* **42** 28–31
- [8] Goebel D M and Katz I 2008 *Fundamentals of Electric Propulsion* (Hoboken, NJ: Wiley)
- [9] Mazouffre S and Lejeune A 2011 High power electric propulsion for robotic exploration of our Solar system *Proc. 1st Int. Conf. on Space Access (Paris)* paper 51
- [10] Koppel C R, Marchandise F, Prioul M, Estublier D and Darnon F 2005 The SMART-1 electric propulsion subsystem around the Moon: in flight experience *Proc. 41th Joint Propulsion Conf. (Tucson, AZ)* AIAA paper 05-3671
- [11] Morozov A I and Savelyev V V 2000 Fundamentals of stationary plasma thruster theory *Rev. Plasma Phys.* vol 21, ed B B Kadomtsev and V D Shafranov (New York: Consultants Bureau) pp 203–391

- [12] Kim V 1998 Main physical features and processes determining the performance of stationary plasma thrusters *J. Propul. Power* **14** 736–43
- [13] Dannenmayer K and Mazouffre S 2011 Elementary scaling relations for Hall effect thrusters *J. Propul. Power* **27** 236–45
- [14] Demtröder W 1998 *Laser Spectroscopy: Basic Concepts and Instrumentation* (Berlin: Springer) pp 367–429
- [15] Sadeghi N 2004 Molecular spectroscopy techniques applied for processing plasma diagnostics *J. Plasma Fusion Res.* **80** 767–76 and references therein
- [16] Biloïu I A, Scime E E and Biloïu C 2009 One- and two-dimensional laser induced fluorescence at oblique incidence *Plasma Sources Sci. Technol.* **18** 025012 and references therein
- [17] Mazouffre S, Kulaev V and Pérez-Luna J 2009 Ion diagnostics of a discharge in crossed electric and magnetic fields for electric propulsion *Plasma Sources Sci. Technol.* **18** 034022
- [18] Gawron D, Mazouffre S, Sadeghi N and Héron A 2008 Influence of magnetic field and discharge voltage on the acceleration layer features in a Hall effect thruster *Plasma Sources Sci. Technol.* **17** 025001
- [19] Hargus W A Jr and Cappelli M A 2001 Laser-induced fluorescence measurements of velocity within a Hall discharge *Appl. Phys. B* **72** 961–9
- [20] Hargus W A Jr and Charles C S 2010 Near-plume laser-induced fluorescence velocity measurements of medium power Hall thruster *J. Propul. Power* **26** 135–41
- [21] Spektor R *et al* 2010 Laser induced fluorescence measurements of the cylindrical Hall thruster plume *Phys. Plasmas* **17** 093502
- [22] MacDonald N A, Cappelli M A, Gildea S R, Martínez-Sánchez M and Hargus W A Jr 2011 Laser-induced fluorescence velocity measurements of a diverging cusped-field thruster *J. Phys. D: Appl. Phys.* **44** 295203
- [23] Lejeune A, Bourgeois G and Mazouffre S 2012 Kr II and Xe II axial velocity distribution functions in a cross-field ion source *Phys. Plasmas* **19** 073501
- [24] Barnat E V 2011 Multi-dimensional optical and laser-based diagnostics of low-temperature ionized plasma discharges *Plasma Sources Sci. Technol.* **20** 053001
- [25] Williams G J *et al* 1999 Laser induced fluorescence measurement of ion velocities in the plume of a Hall effect thruster *Proc. 35th Joint Propulsion Conference (Los Angeles, CA)* AIAA paper 99-2424
- [26] Pawelec E, Mazouffre S and Sadeghi N 2011 Hyperfine structure of some near-infrared Xe I and Xe II lines *Spectroch. Acta B* **66** 470–75
- [27] Mazouffre S, Bourgeois G, Garrigues L and Pawelec E 2011 A comprehensive study on the atom flow in the cross-field discharge of a Hall thruster *J. Phys. D: Appl. Phys.* **44** 105203
- [28] Hargus W A Jr, Azarnia G M and Nakles M R 2001 Demonstration of laser-induced fluorescence on a krypton Hall effect thruster *Proc. 32nd Int. Electric Propulsion Conf. (Wiesbaden)* paper 2011-018
- [29] Hollas J M 1998 *High Resolution Spectroscopy* (New York: Wiley)
- [30] Ngom B B, Smith T B, Huang W and Gallimore A D 2008 Numerical simulation of the Zeeman effect in neutral xenon from NIR diode-laser spectroscopy *J. Appl. Phys.* **104** 023303
- [31] Mazouffre S, Gawron D, Kulaev V and Sadeghi N 2008 Xe<sup>+</sup> ion transport in the crossed-field discharge of a 5 kW class Hall effect thruster *IEEE Trans. Plasma Sci.* **36** 1967–76
- [32] Nakles M R and Hargus W A Jr 2011 Background pressure effects on ion velocity distribution within a medium-power Hall thruster *J. Propul. Power* **27** 737–43
- [33] Garrigues L, Mazouffre S and Bourgeois G 2012 Computed versus measured ion velocity distribution functions in a Hall effect thruster *J. Appl. Phys.* **111** 113301
- [34] Hagelaar G J M, Bareilles J, Garrigues L and Boeuf J P 2003 Role of anomalous electron transport in a stationary plasma thruster simulation *J. Appl. Phys.* **93** 67–75
- [35] Adam J C, Héron A and Laval G 2004 Study of stationary plasma thrusters using two-dimensional fully kinetic simulations *Phys. Plasmas* **11** 295–305
- [36] Mazouffre S, Bourgeois G, Dannenmayer K and Lejeune A 2012 Ionization and acceleration processes in a small, variable channel width, permanent magnet Hall thruster *J. Phys. D: Appl. Phys.* **45** 185203
- [37] Hargus W A Jr and Charles C S 2008 Near exit plane velocity field of a 200-W Hall thruster *J. Propul. Power* **24** 127–33
- [38] Beiting E J and Pollard J E 2000 Measurements of xenon ion velocities of the SPT-140 using laser induced fluorescence *Proc. 3rd Int. Conf. on Spacecraft Propulsion (Cannes)* ESA SP-465, pp 897–900
- [39] Hargus W A Jr 2011 Laser-induced fluorescence-derived Hall effect thruster ion velocity distribution visualization *IEEE Trans. Plasma Sci.* **39** 2918–19
- [40] Hruby H, Monheiser J, Pote B, Rostler P, Lolencik J and Freeman C 1999 Development of low power Hall thrusters *Proc. 30th Plasmadynamics and Lasers Conf. (Norfolk, VA)* AIAA paper 99-3534
- [41] Hargus W A Jr and Cappelli M A 2002 Interior and exterior laser-induced fluorescence and plasma measurements within a Hall thruster *J. Propul. Power* **18** 159–68
- [42] Huang W, Gallimore A D and Smith T B 2011 Two-axis laser-induced fluorescence of singly-charged xenon inside a 6-kW Hall thruster *Proc. 49th Aerospace Sciences Meeting (Orlando, FL)* AIAA paper 2011-1015
- [43] Smirnov A, Raitses Y and Fisch N J 2003 Enhanced ionization in the cylindrical Hall thruster *J. Appl. Phys.* **94** 852–57
- [44] Mazouffre S and Bourgeois G 2010 Spatio-temporal characteristics of ion velocity in a Hall thruster discharge *Plasma Sources Sci. Technol.* **19** 065018
- [45] Pérez-Luna J, Hagelaar G J M, Garrigues L and Boeuf J P 2009 Method to obtain the electric field and the ionization frequency from laser induced fluorescence measurements *Plasma Sources Sci. Technol.* **18** 034008
- [46] Spektor R 2010 Computation of two-dimensional electric field from the ion laser induced fluorescence measurements *Phys. Plasmas* **17** 093503
- [47] Manzella D H 1994 Stationary plasma thruster ion velocity distribution *Proc. 30th Joint Propulsion Conf. (Indianapolis, IN)* AIAA paper 94-3141
- [48] Bourgeois G, Mazouffre S and Sadeghi N 2010 Unexpected transverse velocity component of Xe<sup>+</sup> ions near the exit plane of a Hall thruster *Phys. Plasmas* **17** 113502
- [49] Bourgeois G 2012 Influence de la topologie magnétique, de la cathode et de la section du canal sur l'accélération des ions dans un propulseur à effet Hall *PhD Thesis*, University of Orléans (in French)
- [50] Cedolin R J, Hargus W A Jr, Storm P V, Hanson R K and Cappelli M A 1997 Laser-induced fluorescence study of a xenon Hall thruster *Appl. Phys. B* **65** 459–69
- [51] Huang W and Gallimore A D 2009 Laser-induced fluorescence study of neutral xenon flow evolution inside a 6 kW Hall thruster *Proc. 31st Int. Electric Propulsion Conf. (Ann Arbor, MI)* paper 09-87
- [52] Huang W, Ngom B B and Gallimore A D 2009 Using nonlinear zeeman spectroscopy to obtain *in situ* magnetic field measurement in a Hall thruster *Proc. 31st Int. Electric Propulsion Conf. (Ann Arbor, MI)* paper 09-088

- [53] Smith T B 2003 Deconvolution of ion velocity distributions from laser-induced fluorescence spectra of xenon electrostatic thruster plumes *PhD Dissertation* University of Michigan, MI
- [54] Choueiri E Y 2001 Plasma oscillations in Hall thrusters *Phys. Plasmas* **8** 1411–26
- [55] Boeuf J P and Garrigues L 1998 Low frequency oscillations in a stationary plasma thruster *J. Appl. Phys* **84** 3541–54
- [56] Mazouffre S, Gawron D and Sadeghi N 2009 A time-resolved LIF study on the ion velocity distribution function in a Hall thruster after a fast current disruption *Phys. Plasmas* **16** 043504
- [57] Pellissier B and Sadeghi N 1996 Time-resolved pulse counting lock-in detection of laser induced fluorescence in the presence of a strong background emission *Rev. Sci. Instrum.* **67** 3405–10
- [58] Bourgeois G, Mazouffre S and Sadeghi N 2009 Examination of the temporal characteristics of the electric field in a Hall effect thruster using a photon-counting technique *Proc. 31st Int. Electric Propulsion Conf. (Ann Arbor, MI)* paper 09-111